MNRAS **000**, 1–18 (2010) Preprint 16 October 2015 Compiled using MNRAS LATEX style file v3.0

Chandra Measurements of a Complete Sample of X-ray Luminous Galaxy Clusters: The Luminosity–Mass Relation

P. A. Giles[1⋆], B. J. Maughan[1], H. Dahle[2], M. Bonamente[3,4], D. Landry[3], C. Jones[5], M. Joy[4], S. S. Murray[5], N. van der Pyl[1]

[1] *HH Wills Physics Laboratory, Tyndall Avenue, Bristol, BS8 1TL, UK*
[2] *Institute of Theoretical Astrophysics, University of Oslo, P.O. Box 1029, Blindern, N-0315 Oslo, Norway*
[3] *Physics Department, University of Alabama in Huntsville, Huntsville, AL, U.S.A*
[4] *NASA National Space Science and Technology Center, Huntsville, AL, U.S.A*
[5] *Harvard-Smithsonian Center for Astrophysics, 60 Garden Street, Cambridge, MA 02138, USA*

arXiv:1510.04270v1 [astro-ph.CO] 14 Oct 2015

ABSTRACT

We present the results of work involving a statistically complete sample of 34 galaxy clusters, in the redshift range $0.15 \leq z \leq 0.3$ observed with *Chandra*. We present the calibration of the Mass-Temperature (MT) relation using hydrostatic mass estimates for the most dynamically relaxed clusters, and use this relation as a mass proxy for the full cluster sample. We find that the slope of the MT relation follows the self-similar expectation, and is consistent with previously published relations. We investigate the luminosity-Mass (LM) relation for the cluster sample, utilising a method to fully account for selection biases. We find that the difference in normalisation of the LM relation with and without accounting for selection effects is ≈2. For a cluster of luminosity 10^{45} erg s^{-1}, we find that the mass estimated from the LM relation when we account for selection effects is ≈40% higher compared to the sample LM relation (not accounting for selection effects).

Key words: galaxies: clusters: general - X-rays: galaxies: clusters

1 INTRODUCTION

Clusters of galaxies are the largest gravitationally-collapsed structures in the Universe. Studying properties such as the number density of clusters and details of their growth from the highest density perturbations in the early Universe, offers insight into the underlying cosmology (e.g. Mantz et al. 2008; Vikhlinin et al. 2009b). The study of galaxy clusters has been transformed with the launch of powerful X-ray telescopes such as *Chandra* and *XMM*, which have allowed the study of the X-ray emitting intracluster medium (ICM) with unprecedented detail and accuracy. Cluster properties have been used widely in the determination of cosmological parameters. Cosmological studies utilising clusters include investigating the cluster temperature function (e.g. Henry & Arnaud 1991; Henry 1997; Eke et al. 1998), scaling relations used as a mass proxy such as the luminosity-mass (e.g Reiprich & Böhringer 2002) and the temperature-mass (e.g. Vikhlinin et al. 2006) relations, using the gas mass fraction, f_{gas} (Allen et al. 2008), and the cluster mass function (e.g. Vikhlinin et al. 2009b), to place constraints on various cosmological parameters. Since one of the most important ingredients of these cosmological studies is the cluster mass, large efforts have been undertaken to accurately determine this quantity. One such method involves the construction of radial temperature and gas density profiles of the ICM, and under the assumption of hydrostatic equilibrium, the cluster mass can be determined.

Observations using X-rays have become a well established method of estimating cluster masses, and, at the present time, arguably the most reliable. However, constructing temperature profiles for individual clusters for use in a hydrostatic mass analysis generally require long telescope exposure times, and not is not feasible for large samples of clusters. Therefore, deriving well calibrated scaling relations between simple cluster observables and mass is of crucial importance for using clusters as cosmological probes (e.g. Mantz et al. 2010b). The X-ray luminosity (L) is one of the easiest cluster properties to obtain, and has had a rich history in its scaling with mass (M). Under the assumption of self-similarity (Kaiser 1986), the LM relation (throughout this work we use the notation LM when generally discussing the luminosity-mass relation) is expected to follow a relationship of $L \propto M^{4/3}$. However, observational stud-

⋆ E-mail: P.Giles@bristol.ac.uk

© 2010 The Authors

ies of the *LM* relation have found a slope steeper than the self-similar expectation, ≈2 (Pratt et al. 2009). The most widely accepted theory for the steep slope of the *LM* relation, is due to heating from sources such as supernovae (Sne) and active galactic nuclei (AGN). This causes gas to be expelled from the inner region, hence suppressing the luminosity. This effect should be larger in lower mass systems due to the shallower potential well, which therefore causes the observed steepening of the *LM* relation.

A complication of measuring the *LM* relation is that the cluster samples used are traditionally X-ray selected, with X-ray flux limited samples suffering from two forms of selection bias, Malmquist bias, where higher luminosity clusters are detectable out to higher redshifts and so occupy a larger survey volume, and Eddington bias, where in the presence of intrinsic or statistical scatter in luminosity for a given mass, objects above a flux limit will have above-average luminosities for their mass. Due to the steep slope of the cluster mass function, the Eddington bias is amplified, resulting in a net movement of lower mass objects into a flux limited sample. The consequence of biases on the observed *LM* relation is to bias the normalisation high and the slope low (see Allen, Evrard & Mantz 2011). Therefore, taking these biases into account is paramount when modeling cluster scaling relations, in order to uncover the true nature of any non-gravitational heating which drives departures from self-similar behavior with mass or redshift. Although scaling relation studies have had a rich history, at the present time only a small number of published relations attempt to account for selection biases (e.g Pratt et al. 2009; Vikhlinin et al. 2009a; Bharadwaj et al. 2015; Lovisari et al. 2015), while Mantz et al. (2010a) provides the most robust handling of selection effects to date.

Deriving cluster masses through X-ray observations with the assumption that the ICM is in hydrostatic equilibrium, is not always valid, as some clusters have complex temperature structures due to processes such as merger events. This assumption is thought to be closely satisfied by clusters that are dynamically relaxed. Clusters that appear to host a cool core (CC) are frequently used for mass derivations as they are believed to be dynamically relaxed. Many methods are used to infer the presence of a CC (see Hudson et al. 2010, for a comprehensive study), including measuring the central temperature drop (e.g. O'Hara et al. 2006), the central cooling time (e.g. Bauer et al. 2005; Santos et al. 2010; Mittal et al. 2011), the core entropy (e.g. Comis et al. 2011) and the cuspiness of the gas density profile (Vikhlinin et al. 2007). Frequently, scaling relations involving the cluster mass are used as a mass proxy to calculate the masses of large cluster samples. This first requires constructing scaling relations for dynamically relaxed clusters, and then inferring the cluster masses from these relations. It has been found however that using CC clusters sometimes results in larger scatter of the *LM* scaling relation compared to non-Cool Core (NCC) clusters (e.g. O'Hara et al. 2006). Maughan et al. (2012) found that by defining a cluster sub-sample using clusters appearing both dynamically relaxed and hosting a cool core, the luminosity-temperature (*LT*) relation appears self-similar, compared to unrelaxed and non-cool core clusters. While this method may be the preferred choice for defining sub-samples of clusters for mass derivations, this limits the cluster sample size used for mass calculations.

This paper aims to measure the masses for a complete sample of 35 clusters to measure the X-ray observable–mass scaling relations . We aim to define a sub-sample of clusters that are both dynamically relaxed and host a CC for which the assumption of hydrostatic equilibrium is valid and accurate X-ray masses can be obtained. By constructing scaling relations between X-ray observables and mass for this sub-sample of clusters, these will be used as a mass proxy for the remaining clusters. The outline of the paper is as follows. In Sect. 2 we discuss the sample selection and data analysis. Sect. 3 details the cluster analysis and determines the cool-core and morphological status of each cluster is the sample. Notes on individual clusters are given in Sect. 4. Our results are presented in Sect. 5. The discussion and conclusions are presented in Sect. 6 and Sect. 7 respectively. Throughout this paper we assume a *WMAP*9 cosmology of H_0=69.7 km s^{-1} Mpc^{-1}, Ω_M=0.282 and Ω_Λ=0.718 (Hinshaw et al. 2013).

2 SAMPLE AND DATA PREPARATION

The sample of clusters used in our analysis was defined by the conditions given in Dahle (2006). The sample of clusters represents a volume-limited sample of X-ray luminous clusters taken from the RASS-based, X-ray flux limited ROSAT Brightest Cluster Sample (BCS) of Ebeling et al. (1998) and its low-flux extension (eBCS, Ebeling et al. (2000)). Dahle (2006) imposed a lower cutoff in X-ray luminosity of $L_{X,0.1-2.4keV} = 6 \times 10^{44}$ erg s^{-1} (the limit based upon a cosmology assuming Ω_M=0.3, Ω_Λ=0.7 and h=0.7), corresponding to a sample of 36 clusters within the redshift range $0.15 \leq z \leq 0.30$. Figure 1 plots the luminosity-redshift distribution of the BCS and eBCS, with the yellow shaded region highlighting the region enclosed by the luminosity and redshift cuts defining our sample selection. Note that two of the clusters were dropped from the cluster sample, as detailed below, leading to a final sample of 34 clusters.

The cluster A689 satisfies these selection criteria, but was noted in the original detection as having a significant portion of its flux coming from embedded point sources, and was therefore excluded from the cluster sample. The source of the embedded point source was found to be a central BL-Lac object (Giles et al. 2012), with the re-analysis determining a cluster X-ray luminosity ∼10 times lower than quoted in the BCS, well below the sample cutoff X-ray luminosity. Furthermore, we found that the quoted redshift for the cluster Zw5768 in Ebeling et al. (1998) was incorrect. After further investigation using an updated redshift (see § 4), we determined that the cluster would not satisfy the sample selection, and was subsequently dropped from the cluster sample. For the X-ray analysis we obtained *Chandra* observations to complete the sample and downloaded archived observations of the remaining clusters from the *Chandra* data archive.

All 34 galaxy clusters in this sample were analysed with the CIAO[1] 4.6 software package and CALDB[2] version 4.5.9. We applied standard processing techniques to the level 1 photon lists to generate a level 2 photon lists. We inspected

[1] See http://cxc.harvard.edu/ciao/
[2] See http://cxc.harvard.edu/caldb/

Table 1. Cluster Sample and *Chandra* Observations.

Cluster	R.A. (J2000.0)	Dec. (J2000.0)	z	$Lx_{BCS,0.1-2.4keV}$ (10^{44} ergs s^{-1})	*Chandra* Observations		
					ObsID	Aim Point	Exposure† (ks)
A2204	16 32 47.04	05 34 31.26	0.152	12.51±1.34	6104 7940	I	86.8
RXJ1720.1+2638	17 20 10.08	26 37 29.28	0.164	9.58±1.08	1453 3224 4361	I	45.2
A586	07 32 20.40	31 37 56.28	0.171	6.64±1.30	11723	I	9.91
A1914	14 23 00.96	37 49 33.96	0.171	10.99±1.11	3593	I	18.9
A665	08 30 57.36	65 50 33.36	0.182	9.84±1.54	12286 13201	I	26.4
A115	00 55 50.69	26 24 37.80	0.197	8.90±2.13	13458 13459 15578	I	282
A520	04 54 10.00	02 55 18.16	0.203	8.85±1.99	9424 9425 9426 9430	I	447
A963	10 17 30.36	39 02 53.88	0.206	6.39±1.18	903	S	35.8
A1423	11 57 19.28	33 36 41.08	0.213	6.19±1.34	538 11724	I	35.6
A773	09 17 53.04	51 43 39.36	0.217	8.99±1.35	533 3588 5006	I	40.1
A1763	13 35 18.24	40 59 59.28	0.223	9.32±1.33	3591	I	19.6
A2261	17 22 27.12	32 07 56.64	0.224	11.32±1.55	5007	I	24.1
A1682	13 06 50.40	43 33 26.28	0.226	7.02±1.37	11725	I	19.9
A2111	15 39 41.52	34 25 50.16	0.229	6.83±1.66	544 11726	I	31.2
Zw5247	12 34 18.96	09 46 12.86	0.229	6.32±1.58	11727	I	19.7
A267	01 52 42.14	01 00 41.30	0.230	8.57±1.80	1448	I	7.29
A2219	16 40 20.40	46 42 29.52	0.230	12.74±1.37	14355 14356 14431	I	118
A2390	21 53 36.72	17 41 44.52	0.233	13.43±3.14	4193	S	22.0
Zw2089	09 00 36.96	20 53 40.20	0.235	6.79±1.76	10463	S	40.1
RXJ2129.6+0005	21 29 40.10	00 05 20.91	0.235	11.67±2.92	552 9370	I	39.6
A1835	14 01 10.92	02 52 42.47	0.253	24.49±3.35	6880 6881 7370	I	193.2
A68	00 37 60.09	09 09 33.05	0.255	9.48±2.61	3250	I	9.99
MS1455.0+2232	14 57 15.12	22 20 35.52	0.258	8.41±2.10	4192	I	91.37
A2631	23 37 38.16	00 16 90.11	0.278	8.57±1.80	3248 11728	I	25.9
A1758N	13 32 38.88	50 33 38.88	0.279	7.51±1.61	13997 15538 15540	I	147
A1576	12 36 58.32	63 11 19.68	0.279	7.20±1.80	7938 15127	I	43.1
A697	08 42 57.60	36 21 55.80	0.282	10.57±3.28	4217	I	17.4
RXJ0439.0+0715	04 39 00.67	07 16 30.76	0.285	8.37±2.55	1449 3583	I	20.5
RXJ0437.1+0043	04 37 90.46	00 43 54.15	0.285	7.96±2.34	7900 11729	I	42.5
A611	08 00 56.64	36 03 23.40	0.288	8.86±2.53	3194	S	15.4
Zw7215	15 01 23.04	42 20 54.96	0.290	7.34±1.91	7899	I	13.0
Zw3146	10 23 39.60	04 11 12.88	0.291	17.27±2.94	909 9371	I	78.7
A781	09 20 26.16	30 30 20.52	0.298	11.29±2.82	534 15128	I	45.0
A2552	23 11 33.12	03 38 60.93	0.302	10.08±2.88	11730	I	22.6

Notes. Column 1: Cluster name; Column 2: R.A.; Column 3: DEC; Column 4: Cluster Redshift; Column 5: Luminosity from Ebeling et al. (1998, 2000), converted to a ΛCDM cosmology; Column 6: *Chandra* ObsID; Column 7: *Chandra* aimpoint; Column 8: Cleaned exposure time.

background lightcurves of the observations following the recommendations of Markevitch et al. (2003), to search for possible background fluctuations. The lightcurves were cleaned by 3σ clipping and periods with count rates >20% deviation from the mean rate were rejected. The final cleaned exposure times are listed in Table 1.

In order to take into account the background of each observation, appropriate blank-sky backgrounds were obtained (which are processed identically to the cluster observations) and reprojected onto the sky to match the cluster observation. For background data sets taken after 01 December 2001, the background observations were telemered in VFAINT mode. Therefore, the additional VFAINT cleaning procedure was applied to the source and background data sets[3].

We then followed a method similar to that outlined in Vikhlinin et al. (2006), hereafter V06, in order to improve the accuracy of the background by applying small adjustments to the baseline model. We first corrected for the rate of charged particle events, which has a secular and short-term variation by as much as 30%. We renormalise the background in the 9.5–12 keV band, where the *Chandra* effective area is nearly zero and the observed flux is due entirely to the particle background events. The renormalisation factor was derived by taking the ratio of the observed count rate in the source and background observations respectively. In addition to the particle background, the blank-sky and source observations contain differing contributions from the soft X-ray background, containing a mixture of the Galactic and geocoronal backgrounds, significant at energies $\leq$1 keV. To take into account any difference in this background component between the blank-sky and source observations, spectra were extracted in regions of the field of view free from cluster emission. The spectra were then subtracted, and the residuals modeled in the 0.4-1keV band using an APEC thermal plasma model (Smith et al. 2001), with the abundance set to

[3] See http://cxc.harvard.edu/ciao/why/aciscleanvf.html

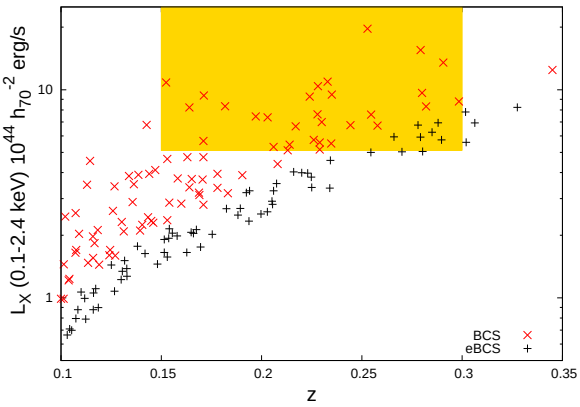

Figure 1. Plot of the luminosity-redshift distribution of the BCS and eBCS clusters. The yellow shaded region highlights the region enclosed by the luminosity and redshift cuts imposed to defined our cluster sample (see § 2).

solar and assuming zero redshift. This component is usually adequately described with a temperature 0.18 keV, however in cases when this produced a poor fit to the residuals the temperature was allowed to be free and then fixed at the value which produced the best fit (see Sect 4 for cases when this was applied). This component was then included in the spectral modeling of the cluster (see § 3.1).

3 DATA ANALYSIS

In this section we detail the data analysis performed on our sample of clusters. The analysis follows closely the analysis presented in Maughan et al. (2012), with any deviations described in the following sections. Since many of the clusters in the sample contained multiple *Chandra* observations, the individual observations were analysed separately as outlined below. The data were then combined for certain stages of the analysis. Source and background spectra were extracted as below for individual observations and fit simultaneously with the temperature of the APEC components tied together.

3.1 Cluster Spectral Properties

Cluster spectra were extracted and fits performed in the 0.6 - 9.0 keV band with an absorbed APEC model, with the absorbing column fixed at the Galactic value (Kalberla et al. 2005) and the abundance allowed to vary. The fits were performed in `XSPEC` (Arnaud 1996) with the spectra containing at least 30 counts per bin, and fit using the χ^2 statistic. The cluster properties were derived within r_{500}, the radius at which the density of the cluster becomes 500 times that of the Universe. Two methods were employed to calculate r_{500} from an estimate of the cluster mass, a hydrostatic mass (M_H) analysis (see §3.4), and the mass determined from the Mass-Temperature (MT) relation (M_T, see §5.1). For the MT relation, each cluster's r_{500} was determined through an iterative process based on the $M_H - T$ relation of the relaxed cool core (RCC) clusters (see §3.5) clusters. We extract a spectrum from within an estimate of r_{500} (using an initial temperature of 5 keV), with the central 15% excluded. A temperature is determined from this spectrum, and a new r_{500} calculated from the $M_H - T$ relation. This process is then iterated until r_{500} converged to within 1%. We denote T as the core excluded temperature, L_{CXO} and L_{bol} as the unabsorbed 0.1–2.4 keV (rest frame) and bolometric luminosities respectively.

3.2 Gas Density Modeling

We make use of the observed projected emissivity profile to accurately measure and model the gas density profile. We converted each annular bin in the surface brightness profile (measured in the 0.7–2.0 keV band) into an integrated emission measure for each annulus. The conversion factor was determined by extracting an ARF and RMF in each annular bin and using these, we simulate a spectrum assuming an absorbed APEC model. The absorption was set at the Galactic value (Kalberla et al. 2005) and the metal abundance set to 0.3 solar. As the data in each annular bin was not sufficient to measure a temperature, the temperature of the model in each bin was obtained by utilizing the average temperature profile found by Vikhlinin et al. (2006), depending on the radius of the bin, the determined r_{500} and the global temperature for each cluster. The normalisation of the spectral model was set to 1 and re-arranged to determine the emission integral for each bin given the derived count rate.

The gas density profile was then fit with a modified version of the standard 1D β-model proposed by V06;

$$n_p n_e = n_0^2 \frac{(r/r_c)^{-\alpha}}{(1+r^2/r_c^2)^{3\beta-\alpha/2}} \frac{1}{(1+r^\gamma/r_s^\gamma)^{\epsilon/\gamma}} \quad (1)$$

We employ the same constraints as employed by V06 i.e. γ is fixed at 3 and $\epsilon < 5$ to exclude nonphysical sharp density breaks. We simplify the model slightly by excluding the second β-model component outlined in V06, so that the model could be used to fit to higher and lower quality data in our sample.

This model was then projected along the line of sight and fit to the observed projected emission measure profile. Gas masses were then determined from Monte Carlo realisations of the projected emissivity profile based on the best fitting projected model to the original data. At each data point, a new randomised point was generated, determined from a Gaussian distribution centered on the model value at that point. The parameters in equation (1) are strongly correlated and therefore the individual parameters degenerate. The individual parameters for each cluster can be found in the appendix (Table A1).

3.3 Temperature Profile Modeling

To determine the total hydrostatic mass of a cluster, we use the method outlined in Vikhlinin et al. (2006). This requires the use of a projected temperature profile. The temperature profile is constructed such that it describes the temperature decline in the central regions of most clusters, and a description for the profile in the outer regions of a cluster. The profile in the central regions of a cluster can be described

as:

$$T_{cool}(r) = \frac{(x + T_{min}/T_0)}{(x+1)}, x = \left(\frac{r}{r_{cool}}\right)^{a_{cool}} \quad (2)$$

Outside the cooling region, the temperature profile can be represented by:

$$T(r) = \frac{(r/r_t)^{-a}}{[1+(r/r_t)^b]^{c/b}} \quad (3)$$

The final three-dimensional temperature profile is then given by:

$$T_{3D}(r) = T_0 T_{cool}(r) T(r) \quad (4)$$

Our clusters are split between relaxed cool core (RCC) and non-relaxed cool core (NRCC) clusters (see Sect. 3.5), and the temperature profiles are constructed in different ways for each subgroup. For the RCC clusters the temperature profiles were constructed by creating concentric annuli centered on the cluster such that each annuli was a specific fraction of the determined r_{500}. To determine the r_{500} for the temperature profile binning, we constructed temperature profiles with each bin containing a minimum of 700 cluster counts. A mass analysis was performed (following § 3.4) using these initial temperature profiles, and an initial r_{500} calculated. Two conditions were then employed to determine the fractions of r_{500} used for the binning temperature profile, 1) the profile had to contain 10 radial bins, and 2) the minimum signal-to-noise of each bin was greater than 20. The annuli were first constructed by using these conditions on our lowest S/N cluster, and then using on the other relaxed clusters, to ensure that these conditions would be met for all the relaxed clusters. This method ensures that the mass estimates for the RCC clusters are derived in a consistent way. Furthermore, the errors on the temperature for each radial bin are converted to account for the fact that the likelihood curve for a measured temperature is approximately Gaussian in log space. We use the method of Andreon (2012) to convert the generally asymmetric errors reported by `XSPEC` into a log-normal likelihood. This is particularly important in the low temperature regions on the outer bins of the temperature profile where the asymmetry in linear space is largest. Due to the varying data quality of the NRCC clusters, we were unable to employ the same r_{500} binning method for the temperature profiles. Therefore, the temperature profiles of the NRCC clusters were constructed such that each bin contained a minimum of 500 cluster counts for each bin (in the 0.7-2.0 keV band).

The temperature profile model (eq 4) is fit to the data by projecting it along the line of sight and computing the χ^2 in the log of the temperature (Table A2 lists the individual fit parameters for our clusters and the figures of the temperature profiles with the corresponding fit are presented). This model has great functional freedom with nine free parameters and can describe many smooth temperature distributions. For cases when the number of bins in the temperature profile is less than the nine free parameters, one or more of the parameters are frozen at values given by the average temperature profile given in V06. The constraints imposed when fitting to a temperature profile with low temperature bins are as follows

(1) No cool core: x=1 and T_0=$T_{\rm min}$ in eq 2.
(2) b=c and a=0.
(3) No cool core, b=c and a=0.

3.4 X-ray Hydrostatic Mass Derivation

To derive the total hydrostatic mass of the cluster, within a radius r, we use the three-dimensional models of the temperature profile, $T(r)$, and gas density profile, obtained by a fit to the emission measure profile converted to a gas density, $\rho_g(r)$, and the hydrostatic equilibrium equation (Sarazin 1988),

$$M(r) = -\frac{kT(r)r}{\mu m_{\rm p} G}\left(\frac{d\,log\,T(r)}{d\,log\,r} + \frac{d\,log\,\rho_{\rm g}(r)}{d\,log\,r}\right) \quad (5)$$

where k is the Boltzmann constant, μ corresponds to a mass weighting appropriate for primordial He abundance (where μ=0.5954) and m_p is the mass of a proton. The gas density profile and temperature profiles are constructed using the method outlined in sections 3.2 and 3.3 respectively.

3.5 Determining the Cool-Core state of a cluster

Here we wish to determine which clusters in our sample appear dynamically relaxed and host a CC (RCC). These clusters can then be assumed to be in hydrostatic equilibrium and masses can be obtained for these clusters. The masses of the remaining clusters can then be determined through derived scaling relations of our RCC clusters.

We employ two methods of determining whether a cluster hosts a cool-core. In a comprehensive study, Hudson et al. (2010) tested 16 cool core probes, and concluded that for high quality data a direct measurement of the central cooling time (CCT) is the preferred probe. Many of the clusters within our sample have high quality data and a reliable measurement of the CCT can be obtained. However, for lower quality data the cuspiness of the gas density profile is the preferred choice. We utilise both of these probes to derive our cool-core sub-sample of clusters.

To derive the CCT of our clusters, we use the equation given in Sarazin (1988).

$$t_{\rm cool} = 8.5\times10^{10}{\rm yr}\left(\frac{n_{\rm p}}{10^{-3}}\right)^{-1}(0.079kT_{\rm CCT})^{1/2} \quad (6)$$

where $n_{\rm p}$=$\sqrt{(1.17{\rm n_p n_e})}$, and $n_p n_e$ is measured using the best fitting gas density models given in § 3.2. $\rm kT_{CCT}$ is measured by extracting a spectrum within [0-0.048]r_{500} (the radius defined in Hudson et al. 2010) and fit with an absorbed APEC model and the addition of the background model from Section 2. The errors on $t_{\rm cool}$ were derived from Gaussian randomisations centered on the $\rm kT_{CCT}$ and within the error bars determined from the spectral fit. Cuspiness is defined as the logarithmic slope of the gas density profile at a radius of $0.04r_{500}$, and is modeled using the best fitting gas density models (§ 3.2).

In order to determine which clusters in our sample contained a cool core, we used the cuts defined in Hudson et al. (2010) for the cuspiness and $\rm t_{cool}$ parameters. Clusters in our sample are determined to have a cool core if they have a cuspiness value greater than 0.7, and $\rm t_{cool}$ less than 7.7Gyr. The values of cuspiness and $\rm t_{cool}$ are given in Table 2.

Now that we have determined which clusters host a cool core, we next determine which clusters in our sample are dynamically relaxed. The dynamical state of the cluster

was measured using the centroid shift ($\langle w \rangle$), following the method of Poole et al. (2006). The centroid shift was defined as the standard deviation of the distance between the X-ray peak and the centroid. The centroid was measured within a series of circular apertures centered on the X-ray peak and decreasing in steps of 5% from r_{500} to $0.05r_{500}$, with the errors derived from 100 Monte Carlo randomisations of the input image with pixels randomised under a Poisson distribution. The values of $\langle w \rangle$ are given in table 2. We make a cut at $\langle w \rangle$=0.009, above which clusters are classed as dynamically unrelaxed, and below which clusters are classed as dynamically relaxed. This value was chosen when visually inspecting images of each cluster ranked in order of $\langle w \rangle$, and seeing a clear change in the structure of the clusters above this value.

We plot t_{cool} against cuspiness in Figure 2, left plot, and cuspiness and t_{cool} against $\langle w \rangle$ in the middle and right plots respectively. In each plot, the RCC sample and NRCC sample are given by the red and blue open circles respectively, and the cuts in cuspiness, t_{cool} and $\langle w \rangle$ are shown by the black dashed lines. We note that the cluster A611 had residual flaring in the background lightcurve and therefore the properties of the cluster could only be derived out to a radius of $\approx 150''$ (see Sect. 4). A reliable hydrostatic mass estimate for this cluster could not be determined, and it was therefore dropped from the RCC sample. Using the cuts described above, we find 10/34 clusters classed as RCC and 24/34 clusters classed as NRCC.

Table 2. Dynamical properties of the cluster sample. Cuspiness is the logarithmic slope of the gas density profile at $0.04r_{500}$; t_{cool} is the cooling time measured within $0.048r_{500}$; and $\langle w \rangle$ is the centroid shift. † Denotes clusters in the RCC sample. (see Sect. 3.5).

Cluster	Cuspiness	t_{cool} (Gyr)	$\langle w \rangle$ $10^{-3}r_{500}$
A2204†	$1.25^{+0.00}_{-0.00}$	$2.03^{+0.01}_{-0.01}$	0.55±0.07
RXJ1720.1+2638†	$1.08^{+0.01}_{-0.01}$	$2.36^{+0.02}_{-0.02}$	1.01±0.21
A586	$0.38^{+0.07}_{-0.07}$	$4.86^{+0.30}_{-0.28}$	9.16±4.45
A1914	$0.26^{+0.02}_{-0.01}$	$7.20^{+0.29}_{-0.26}$	13.7±1.28
A665	$0.55^{+0.02}_{-0.01}$	$8.33^{+0.18}_{-0.16}$	40.9±1.33
A115	$1.04^{+0.01}_{-0.01}$	$2.57^{+0.02}_{-0.02}$	86.9±0.33
A520	$0.04^{+0.02}_{-0.00}$	$22.6^{+0.63}_{-0.65}$	53.6±3.04
A963	$0.63^{+0.02}_{-0.02}$	$3.74^{+0.08}_{-0.08}$	2.42±1.36
A1423†	$0.80^{+0.03}_{-0.03}$	$3.34^{+0.11}_{-0.10}$	6.11±1.61
A773	$0.24^{+0.06}_{-0.03}$	$10.0^{+0.56}_{-0.54}$	6.27±2.02
A1763	$0.23^{+0.07}_{-0.03}$	$11.1^{+1.17}_{-1.06}$	5.14±3.87
A2261	$0.65^{+0.03}_{-0.03}$	$3.11^{+0.09}_{-0.10}$	9.27±1.02
A1682	$0.42^{+0.08}_{-0.11}$	$8.07^{+1.46}_{-1.08}$	38.6±3.31
A2111	$0.15^{+0.11}_{-0.05}$	$11.1^{+0.94}_{-1.12}$	30.1±11.3
Zw5247	$0.55^{+0.07}_{-0.12}$	$20.9^{+2.99}_{-2.70}$	59.8±28.3
A267	$0.19^{+0.15}_{-0.04}$	$5.67^{+0.71}_{-0.74}$	26.2±14.1
A2219	$0.30^{+0.03}_{-0.04}$	$10.2^{+0.39}_{-0.32}$	14.7±4.81
A2390	$0.99^{+0.01}_{-0.02}$	$5.37^{+0.05}_{-0.05}$	9.81±0.20
Zw2089†	$1.10^{+0.02}_{-0.01}$	$1.01^{+0.01}_{-0.01}$	4.87±0.71
RXJ2129.6+0005†	$1.01^{+0.01}_{-0.01}$	$1.70^{+0.03}_{-0.03}$	8.37±1.78
A1835†	$1.22^{+0.00}_{-0.00}$	$1.19^{+0.01}_{-0.01}$	2.73±0.43
A68	$0.31^{+0.12}_{-0.12}$	$12.0^{+2.09}_{-1.99}$	10.4±2.92
MS1455.0+2232†	$1.01^{+0.01}_{-0.01}$	$0.95^{+0.01}_{-0.01}$	4.01±0.28
A2631	$0.25^{+0.09}_{-0.11}$	$12.5^{+2.31}_{-1.89}$	23.2±8.04
A1758N	$0.02^{+0.02}_{-0.01}$	$24.4^{+1.43}_{-1.31}$	15.3±5.20
A1576	$0.35^{+0.07}_{-0.03}$	$7.29^{+0.48}_{-0.51}$	13.4±3.11
A697	$0.20^{+0.08}_{-0.03}$	$11.0^{+1.27}_{-1.29}$	5.41±1.24
RXJ0439.0+0715†	$0.78^{+0.04}_{-0.04}$	$3.30^{+0.16}_{-0.14}$	5.42±2.30
RXJ0437.1+0043†	$0.83^{+0.05}_{-0.06}$	$1.96^{+0.09}_{-0.07}$	6.25±2.24
A611	$0.72^{+0.04}_{-0.03}$	$2.93^{+0.18}_{-0.09}$	6.38±1.19
Zw3146†	$1.01^{+0.01}_{-0.01}$	$0.82^{+0.01}_{-0.01}$	3.25±0.31
Zw7215	$0.13^{+0.25}_{-0.04}$	$12.7^{+1.29}_{-1.35}$	31.5±12.5
A781	$0.03^{+0.18}_{-0.02}$	$32.1^{+8.93}_{-9.15}$	59.2±3.94
A2552	$0.50^{+0.07}_{-0.08}$	$4.92^{+0.47}_{-0.45}$	5.02±1.38

4 NOTES ON INDIVIDUAL CLUSTERS

In this section we note any peculiarities or points of interest for observations in which we departed from the described analysis process.

A586 – ObsID 530 was rejected due to long, low level flaring, leaving ObsID 11723.

A665 – We reject ObsID 531 due to large temperature required to fit soft background residuals (0.6 keV). We reject ObsID 3586 due to several periods of high background. We reject ObsID 7700 due to energy filters placed on the observation. This leaves ObsIDs 12286 and 13201, both ≈50ks observations.

A115 – This cluster is undergoing a major off-axis merger, with two sub-clusters separated by 300″ (1 Mpc) in projection. Two regions were manually excluded from the analysis to exclude emission from the southern subcluster. Sources were excluded at $\alpha[2000.0] = 00^h55^m58.89^s$, $\delta[2000.0] = +26°19'28.45''$ and $\alpha[2000.0] = 00^h56^m03.78^s$, $\delta[2000.0] = +26°22'44.48''$, with radii 182″ and 63″ respectively.

A963 – A temperature of 0.32 keV was used when fitting an APEC model to the soft background residuals.

A1763 – An extended source at $\alpha[2000.0] = 13^h34^m55.29^s$, $\delta[2000.0] = +40°57'22.93''$, 304″ from the cluster core was manually excluded. The extended emission is likely associated with a known X-ray source (Evans et al. 2010).

A2261 – A small extended source at $\alpha[2000.0] = 17^h22^m12.15^s$, $\delta[2000.0] = +32°06'54.0''$, 200″ from the cluster core was manually excluded. The extended emission is associated with a known galaxy at a photo-z=0.304 (Hao et al. 2010).

A1682 – ObsID 2344 was rejected due to high flare periods, leaving ObsID 11725.

A2111 – This cluster has been shown to be undergoing a head-on merger with a subcluster, appearing as a comet-shaped X-ray subcomponent and hotter than the surrounding gas (Wang, Ulmer & Lavery 1997). A region at $\alpha[2000.0] = 15^h39^m32.68^s$, $\delta[2000.0] = +34°28'04.79''$, 210″ from the cluster core was manually excluded to exclude the emission from the merger.

Zw5247 – ObsID 539 was rejected due to long, low level flaring, leaving ObsID 11727. This system consists of a binary merger of two clusters of similar mass. Only one redshift is given in Ebeling et al. (1998), corresponding to the position of the southern subcluster. For this reason the northern sub cluster was manually excluded from our analysis using a box region at $\alpha[2000.0] = 12^h34^m33.18^s$, $\delta[2000.0] = +09°49'52.84''$ of length 428×421″.

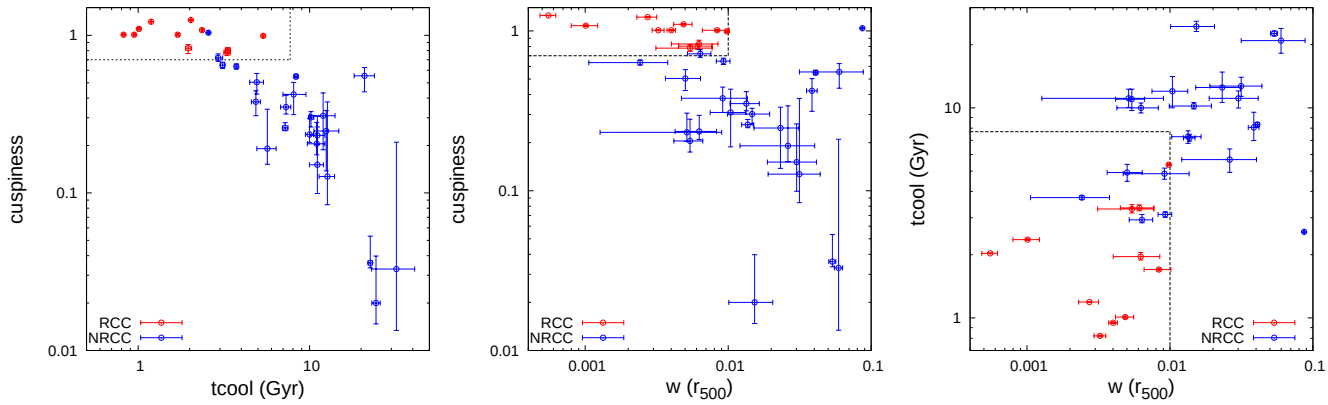

Figure 2. Left: Plot of t_{cool} against $\langle w \rangle$ with the dashed horizontal line the cut at t_{cool}=6.5 and the dashed vertical line the cut at $\langle w \rangle$=0.009r_{500}, Middle: Plot of cuspiness against $\langle w \rangle$ with the dashed horizontal line the cut at cuspiness=0.65 and the dashed vertical line the cut at $\langle w \rangle$=0.009r_{500}, Right: Plot of cuspiness against t_{cool} with the dashed horizontal line the cut at cuspiness=0.65 and the dashed vertical line the cut at t_{cool}=6.5. The red hollow circles represent the RCC clusters, blue hollow squares represent the NRCC clusters. The cluster at $\langle w \rangle$=0.087 is the double cool-core cluster A115.

A267 – ObsID 3580 was rejected due to long, low level flaring leaving ObsID 1448.

A2390 – We discard ObsID 500 and 501 as both observations were taken in FAINT mode, which results in poorer background rejection, leaving ObsID 4192. A temperature of 0.25 keV was used when fitting an APEC model to the soft background residuals.

MS1455.0+2232 – For ObsID 4192 we used a temperature of 0.21 keV when fitting an APEC model to the soft background residuals.

Zw5768 – The cluster redshift was given as z=0.266 in Ebeling et al. (2000). This was found to be incorrect, with Böhringer et al. (2000) reporting a spectroscopic redshift of z=0.171. To check this we searched the SDSS DR7 release and found the redshift of the BCG of the cluster to be z=0.172. However, we found that the measured luminosity of the cluster was significantly lower than the luminosity cut used to define our cluster sample. The luminosity measured in the 0.1–2.4 keV band out to a radius of 1.43 Mpc (consistent with Ebeling et al. 2000), including the cluster core and correcting to an H_0=50 km s^{-1} Mpc^{-1} was $L_{0.1-2.4keV}$=(1.36±0.07)×10^{44} ergs s^{-1}. This calculated luminosity is also consistent with that given in Böhringer et al. (2000) of L_X=1.67×10^{44} ergs s^{-1} (no error given). This cluster was subsequently dropped from the cluster sample.

A1758N – ObsId 7710 was excluded due to energy filters placed on the observation and residual flaring in the observation. ObsID 2213 was excluded due to large residual flaring in the observation. The cluster A1758S was excluded manually from the analysis, using a circle region centered at α[2000.0] = $13^h32^m32.04^s$, δ[2000.0] = +50°24′32.95″.

RXJ0439.0+0715 – We excluded the first 6ks of the observation of ObsID 3583 due to flaring.

A611 – We excluded the first 22ks of the observation due to long low level flaring. Periods of high background were still present in the observation and therefore the cluster temperature was extracted out to a radius of ≈150″, and this was assumed to be the average cluster temperature (kT = $8.41^{+0.93}_{-0.75}$ keV). The cluster properties were then extracted within a radius of r_{500} determined following the procedure outlined in §3.1, with the temperature fixed at the value above.

Zw3146 – For ObsID 9371 we used a temperature of 0.26 keV when fitting an APEC model to the soft background residuals.

A2552 – ObsID 3288 was rejected due to high flare periods, leaving ObsID 11730. An extended source, identified as the galaxy cluster NSCS J231153+034038 at z=0.36 (Lopes et al. 2004), at α[2000.0] = $23^h11^m48.3^s$, δ[2000.0] = +03°40′47.1″, 276″ from the cluster core was manually excluded.

5 X-RAY SCALING RELATIONS

Establishing the relationship between total mass and observable quantities is a critical step for the derivation of cosmological parameters using galaxy clusters. Scaling relations using simple cluster observables such as the X-ray luminosity, gas mass, temperature and the Y_X parameter (the product of the gas mass and temperature), provide useful proxies for cluster mass. In this work we focus on the scaling of the luminosity and temperature with mass. The scaling relations are split between the RCC and NRCC subsets defined in section 3.5. We first present the mass-temperature relation ($M_H - T$), where M_H denotes hydrostatic masses. The $M_H - T$ relation for the RCC clusters is then used as a mass proxy for the whole sample. We then investigate the form of the luminosity-mass relation, focusing on the sample relation (not accounting for biases), and the bias-corrected relation.

5.1 The Mass-Temperature relation

The mass-temperature (MT) relation has been widely used for the calibration of cluster masses using relaxed galaxy clusters (e.g. Arnaud, Pointecouteau & Pratt 2005; Vikhlinin et al. 2006). We use the $M_H - T$ relation as a mass

Table 3. X-ray Properties of our cluster sample. The properties are derived within r_{500} determined from the RCC $M_H - T$ relation (see §5.1). † Indicates RCC clusters.

Cluster	$r_{T,500}$ (Mpc)	L_{CXO} (10^{44} ergs s^{-1})	L_{bol} (10^{44} ergs s^{-1})	T (keV)	M_T (10^{14}M$_\odot$)
A2204†	$1.41^{+0.05}_{-0.05}$	16.19±0.06	42.32±0.14	$9.15^{+0.43}_{-0.44}$	$9.15^{+0.91}_{-0.92}$
RXJ1720.1+2638†	$1.32^{+0.04}_{-0.04}$	9.35±0.10	22.34±0.23	$7.98^{+0.38}_{-0.39}$	$7.57^{+0.68}_{-0.68}$
A586	$1.13^{+0.06}_{-0.06}$	5.35±0.13	12.64±0.3	$5.75^{+0.68}_{-0.63}$	$4.80^{+0.82}_{-0.77}$
A1914	$1.43^{+0.06}_{-0.06}$	11.72±0.11	36.92±0.34	$9.49^{+0.58}_{-0.59}$	$9.63^{+1.12}_{-1.13}$
A665	$1.39^{+0.05}_{-0.04}$	8.35±0.05	23.34±0.15	$8.88^{+0.53}_{-0.42}$	$8.78^{+0.96}_{-0.85}$
A115	$1.25^{+0.04}_{-0.04}$	5.67±0.04	12.37±0.08	$7.17^{+0.36}_{-0.41}$	$6.52^{+0.56}_{-0.61}$
A520	$1.31^{+0.03}_{-0.03}$	6.91±0.03	18.58±0.09	$7.91^{+0.27}_{-0.27}$	$7.47^{+0.56}_{-0.57}$
A963	$1.11^{+0.04}_{-0.03}$	6.62±0.07	15.39±0.15	$5.67^{+0.32}_{-0.31}$	$4.70^{+0.45}_{-0.44}$
A1423†	$1.15^{+0.04}_{-0.04}$	5.23±0.08	11.70±0.17	$6.14^{+0.41}_{-0.41}$	$5.25^{+0.55}_{-0.55}$
A773	$1.32^{+0.04}_{-0.04}$	6.84±0.10	18.97±0.27	$8.22^{+0.41}_{-0.41}$	$7.88^{+0.73}_{-0.74}$
A1763	$1.36^{+0.06}_{-0.05}$	8.03±0.12	22.90±0.33	$8.87^{+0.73}_{-0.57}$	$8.76^{+1.19}_{-1.00}$
A2261	$1.31^{+0.04}_{-0.04}$	11.25±0.12	30.67±0.32	$8.19^{+0.43}_{-0.43}$	$7.84^{+0.75}_{-0.75}$
A1682	$1.15^{+0.06}_{-0.06}$	4.29±0.11	10.15±0.26	$6.14^{+0.64}_{-0.65}$	$5.26^{+0.81}_{-0.81}$
A2111	$1.27^{+0.06}_{-0.06}$	4.58±0.08	11.92±0.21	$7.66^{+0.73}_{-0.73}$	$7.15^{+1.03}_{-1.03}$
Zw 5247	$1.06^{+0.06}_{-0.06}$	2.83±0.13	5.98±0.26	$5.19^{+0.57}_{-0.54}$	$4.16^{+0.68}_{-0.65}$
A267	$1.03^{+0.05}_{-0.05}$	5.81±0.21	12.19±0.45	$4.85^{+0.44}_{-0.44}$	$3.79^{+0.54}_{-0.54}$
A2219	$1.53^{+0.06}_{-0.01}$	16.81±0.11	56.87±0.38	$11.39^{+0.49}_{-0.50}$	$12.40^{+1.53}_{-0.15}$
A2390	$1.52^{+0.07}_{-0.08}$	17.39±0.09	59.09±0.31	$11.26^{+0.72}_{-0.90}$	$12.21^{+1.69}_{-1.87}$
Zw 2089†	$0.97^{+0.06}_{-0.05}$	6.09±0.09	10.82±0.17	$4.31^{+0.52}_{-0.37}$	$3.21^{+0.60}_{-0.46}$
RXJ2129.6+0005†	$1.19^{+0.04}_{-0.04}$	9.42±0.10	21.80±0.23	$6.66^{+0.40}_{-0.37}$	$5.89^{+0.57}_{-0.54}$
A1835†	$1.42^{+0.05}_{-0.05}$	22.41±0.07	59.65±0.19	$9.86^{+0.42}_{-0.43}$	$10.15^{+1.05}_{-1.06}$
A68	$1.31^{+0.09}_{-0.08}$	6.35±0.17	19.18±0.51	$8.27^{+1.12}_{-0.98}$	$7.95^{+1.58}_{-1.40}$
MS1455.0+2232†	$1.07^{+0.03}_{-0.03}$	10.95±0.08	22.26±0.17	$5.40^{+0.29}_{-0.22}$	$4.40^{+0.41}_{-0.35}$
A2631	$1.20^{+0.05}_{-0.04}$	7.76±0.13	20.44±0.33	$7.01^{+0.57}_{-0.38}$	$6.31^{+0.78}_{-0.57}$
A1758	$1.31^{+0.04}_{-0.03}$	8.50±0.10	23.49±0.27	$8.61^{+0.30}_{-0.25}$	$8.40^{+0.70}_{-0.66}$
A1576	$1.24^{+0.06}_{-0.06}$	6.03±0.09	16.61±0.25	$7.53^{+0.66}_{-0.66}$	$6.98^{+0.93}_{-0.93}$
A697	$1.55^{+0.10}_{-0.10}$	13.45±0.23	45.78±0.79	$12.29^{+1.22}_{-1.25}$	$13.79^{+2.55}_{-2.58}$
RXJ0439.0+0715†	$1.17^{+0.04}_{-0.04}$	7.22±0.12	16.91±0.28	$6.40^{+0.45}_{-0.45}$	$5.56^{+0.61}_{-0.61}$
RXJ0437.1+0043†	$1.23^{+0.06}_{-0.06}$	7.63±0.11	18.18±0.27	$7.41^{+0.78}_{-0.78}$	$6.82^{+1.06}_{-1.07}$
A611	$1.31^{+0.08}_{-0.06}$	7.11±0.15	18.76±0.4	$8.47^{+0.97}_{-0.75}$	$8.31^{+1.46}_{-1.13}$
Zw 3146†	$1.21^{+0.11}_{-0.09}$	4.76±0.16	12.18±0.42	$7.16^{+1.32}_{-1.08}$	$6.51^{+1.70}_{-1.41}$
Zw 7215	$1.30^{+0.04}_{-0.04}$	20.27±0.11	48.41±0.27	$8.29^{+0.37}_{-0.37}$	$7.97^{+0.71}_{-0.71}$
A781	$1.15^{+0.04}_{-0.04}$	5.10±0.09	12.23±0.21	$6.43^{+0.37}_{-0.37}$	$5.61^{+0.53}_{-0.53}$
A2552	$1.31^{+0.07}_{-0.06}$	8.98±0.16	25.07±0.45	$8.53^{+0.86}_{-0.77}$	$8.30^{+1.29}_{-1.18}$

calibrator since this relation is not strongly influenced by selection effects (Mantz et al. 2010b). We do not investigate in this work scaling relations involving the gas mass (e.g. the Y_X-mass relation), since the gas mass may be influenced by selection effects. The hydrostatic masses and temperatures used in this relation can be found in Table B1. Figure 3, left plot, shows the $M_H - T$ relation for our RCC clusters. We fit a power law of the form

$$E(z)^{\gamma_{MT}} M = A_{MT} \left(\frac{T}{T_0} \right)^{\alpha_{MT}} \quad (7)$$

assuming T_0=7 keV and γ_{MT}=1 (the self-similar expectation). A power law was fit to the data using the BCES orthogonal regression in log space (Akritas & Bershady 1996), finding a normalisation of $A_{MT} = (5.09 \pm 0.25) \times 10^{14} M_\odot$, slope of $\alpha_{MT} = 1.39 \pm 0.14$ and scatter $\sigma_{MT} = 0.25 \pm 0.32$. We compare to the MT relations given in Arnaud, Pointecouteau & Pratt (2007) and Vikhlinin et al. (2009a), represented by the green dashed and pink dotted lines in Figure 3 respectively.

In the right plot of Figure 3 we overplot the $M_H - T$ relation of the NRCC clusters, given by the blue squares. We note that due to the departure from hydrostatic equilibrium for these clusters, due to processes such as cluster mergers, the hydrostatic mass estimate is likely to be unreliable. Fitting a power law to the data, we find $A_{MT} = (4.46 \pm 0.41) \times 10^{14} M_\odot$, slope of $\alpha_{MT} = 1.97 \pm 0.32$ and scatter $\sigma_{MT} = 0.11 \pm 0.08$. Due to the increased slope and scatter of the hydrostatic NRCC MT relation, we use the RCC $M_H - T$ relation as a mass proxy for the NRCC clusters. Our analysis will therefore focus on masses derived using the RCC $M_H - T$ relation for the entire cluster sample, providing consistency. The masses were estimated via the iterative process described in Section 3.1, and the errors on the temperature and RCC $M_H - T$ relation added in quadrature to give the error on the mass. Table 3 gives the properties of

Table 4. Best fitting parameters for $M_H - T$ relations. Scaling relations are fit by a powerlaw of the form $E(z)^{\gamma_{MT}} M = A_{MT}(T/T_0)^{\alpha_{MT}}$, where $A_{MT} = 6$ keV.

Relation	A_{MT} (10^{14})	B_{MT}	δ_{MT}
RCC, $M_H - T$	5.09 ± 0.25	1.39 ± 0.14	0.25 ± 0.32
NRCC, $M_H - T$	4.46 ± 0.41	1.97 ± 0.32	0.11 ± 0.08
ALL, $M_H - T$	4.70 ± 0.26	1.79 ± 0.21	0.05 ± 0.06

our cluster sample, derived within the r_{500} determined from the RCC $M_H - T$ above.

5.2 The sample L_{CXO}-M_T relation

Here we derive the luminosity–mass (LM) relation for our clusters. Due to the relative ease of measuring the X-ray luminosity of clusters, scaling relations involving the luminosity have had a rich history (e.g. Mitchell, Ives & Culhane 1977; Arnaud & Evrard 1999; Reiprich & Böhringer 2002; Pratt et al. 2009; Maughan et al. 2012). Figure 4 shows our derived $L_{CXO} - M_T$ relation (where M_T is the masses derived from the RCC $M_H - T$ relation) split between our RCC sample (red open circles) and NRCC sample (blue open squares). The luminosities are derived in the [0-1]r_{500} range for consistency with the comparison to the bias-corrected L_{CXO}-M_T relation (see § 5.4).

We fit to the data a power law relation of the form

$$E(z)^{\gamma_{\rm LM}} \left(\frac{L_{CXO}}{L_0}\right) = A_{\rm LM} \left(\frac{M_T}{M_0}\right)^{\alpha_{\rm LM}} \quad (8)$$

assuming $L_0 = 10^{45}$ ergs s^{-1}, $M_0 = 10^{15} M_\odot$ and $\gamma_{LM} = -7/3$ (the self-similar expectation). We find a normalisation and slope of $A_{LM} = (9.68 \pm 0.66) \times 10^{44}$ ergs s^{-1} and $\alpha_{\rm LM}$=1.36±0.56 for the RCC sample, and $A_{LM} = (8.28 \pm 0.29) \times 10^{44}$ ergs s^{-1} and $\alpha_{\rm LM} = 1.38 \pm 0.07$ for the NRCC sample. We find that the normalisation of the NRCC sample is 1.19±0.09 times lower than that of the RCC sample (significant at the 1.9σ level), however this is unsurprising due to the large increase in luminosity towards the centers of cool core clusters. We compare to the LM relation given in Pratt et al. (2009), appropriate for core included luminosities in the 0.1–2.4 keV band (see Table A.2 in Pratt et al. 2009). The Pratt et al. (2009) LM relation is given by the dashed-dotted cyan line in Figure 4, where we find no significant difference to our L_{CXO}-M_T relation.

5.3 Selection Function

The sample was selected to match that in Dahle (2006), who selected the clusters from the (e)BCS in the redshift range $0.150 < z < 0.303$ based on the soft-band ($0.1 - 2.4$ keV) luminosity as measured in the BCS, $L^{EdS}_{BCS} > 10^{45}$ erg s^{-1}. However (as we indicate with the EdS superscript), the BCS luminosities were computed assuming an Einstein de-Sitter cosmology ($\Omega_M = 1$, $\Omega_\Lambda = 0$, $H_0 = 50$ km s^{-1} Mpc^{-1}), so in order to work in our preferred ΛCDM cosmology it was necessary to convert the BCS luminosities and our selection function to this cosmology. The ΛCDM selection function $L_{lim}(z)$ is well approximated by $L_{BCS} > 5.26 \times 10^{44} \times 10^{0.324z}$ erg s^{-1}, where L_{BCS} (i.e. without an EdS superscript) indicates the soft band BCS luminosity in our ΛCDM cosmology.

The completeness of the BCS survey is a function of flux, but the full selection function has not been published. However, completeness estimates at specific fluxes are given in Ebeling et al. (1998) and Ebeling et al. (2000), and so we modeled the survey completeness as a logistic function of the form

$$P(I|f) = \left(1 + e^{-0.7(f-1.2)}\right)^{-1} \quad (9)$$

where $P(I|f)$ is the probability that a cluster with a normalised (e)BCS 0.1−2.4keV flux $f = F_{BCS}/(10^{-12}$ erg s$^{-1})$ is included in the sample. The numerical constants in this model were determined from a simple fit by eye of the logistic function to the published (e)BCS completeness values, as illustrated in Figure 5. This functional approximation is within 0.01 in $P(I|f)$ of the published completeness values.

5.4 The bias-corrected L_{CXO}-M_T relation

The preceding fit of the observed $L_{CXO} - M_T$ relation (§ 5.2) represents an accurate description of the correlation between luminosity and mass for our subsample. However, in order to compute an unbiased estimate of the population $L_{CXO} - M_T$ relation, care must be taken to avoid the effects of selection biases (see Allen, Evrard & Mantz 2011, for a discussion). Our analysis is based closely on that of Mantz et al. (2010b), which presents the most complete treatment of selection biases in X-ray cluster surveys and their effects on scaling relations and cosmological studies.

One way to visualise the steps required to correct for the selection biases is to consider how one would realistically generate a synthetic population like that being studied. In our case the steps would be: (i) to use a model mass function $\phi = dN/dMdV$ to predict the number of clusters as a function of mass and redshift in the volume studied; (ii) to then generate a Poissonian realisation of that population, and assign each cluster a luminosity L_{BCS} based on its mass and redshift, according to a model LM relation; (iii) next, intrinsic scatter at the appropriate level (a lognormal with standard deviation σ_{LM}) would be added to the assigned L values; (iv) fluxes could then be computed for each cluster, using assumptions about the temperature and metal abundance (and their mass dependence) to allow k-correction of the fluxes into the observed frame (F_{BCS}); (v) statistical scatter would then be added to those luminosities and fluxes, requiring a model predicting the size of the statistical error for a given flux (e.g. by converting the flux to number of counts for a mean exposure time, and assuming Poisson errors); (vi) finally, the sample selection would be applied, rejecting all clusters fainter than $L_{lim}(z)$, and discarding clusters probabilistically as a function of their flux according to $P(I|f)$. At stage (v) secondary observations (such as our *Chandra* follow-up observations) can be generated by computing a *Chandra* luminosity with its own statistical uncertainty, and possibly including a cross-calibration scaling between *ROSAT* and *Chandra*.

Considering this procedure for simulating data with properties close to the true population gives insight into the likelihood function of the data (the probability of the data

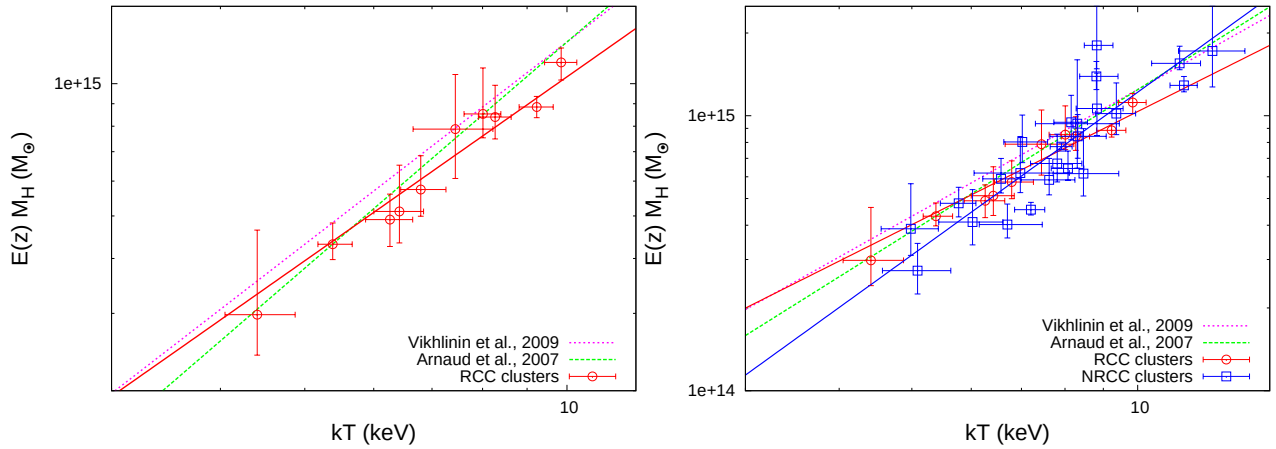

Figure 3. Left: The $M_H - T$ relation for the RCC sample. The clusters are highlighted by the red open circles, with the corresponding power law fit given by the red solid line. The relations of Arnaud, Pointecouteau & Pratt (2007) and Vikhlinin et al. (2009a), are given by the green dashed and pink dotted lines respectively; Right: Same as the left plot, but with the NRCC clusters overplotted, with the corresponding power law fit given by the blue solid line

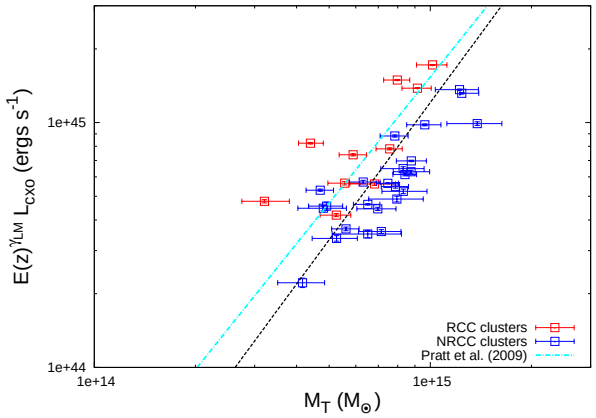

Figure 4. The $L_{CXO} - M_T$ relation for our clusters, with the masses derived from the RCC $M_H - T$ relation. The clusters are split between the RCC (red open squares) and NRCC (blue open squares) samples. The corresponding BCES fit (see § 5.2) to the clusters is given by the black dashed line. The LT relation of Pratt et al. (2009) is given by the dotted-dashed cyan line.

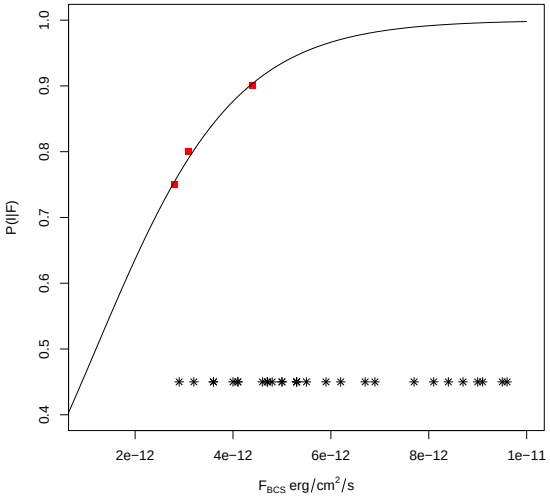

Figure 5. Our logistic function approximation to the (e)BCS completeness as a function of (e)BCS flux is plotted with the published completeness values for the (e)BCS survey (red squares). The asterisk symbols indicate the F_{BCS} of the clusters in our sample, and are at arbitrary completeness.

being observed given a model and its parameter values). The likelihood is the inverse of the steps needed to simulate the data. For the LM relation, the final likelihood thus depends on the likelihood of the number of clusters detected in the subsample (and by extension the number omitted), and the likelihood of the detected clusters having their observed properties. In the following sections we derive the likelihood for the LM relation and describe our specific implementation of this in fitting to our sample.

5.4.1 The likelihood function for the LM relation

The number of clusters predicted by our model to be observed in the subsample defined by our selection function is the integral of the mass function over the volume over the survey, weighted by the probability that a cluster of a given mass would be included in the subsample given the LM relation and the intrinsic and statistical scatter on the luminosity. Using the notation that observed quantities are denoted with a hat, this is expressed as

$$\langle N_{det} \rangle = \int dM \int dz\, \phi(M,z) \frac{dV}{dz} \Omega \times \int dL\, P(L_{BCS}|M) \times \int d\hat{L}_{BCS}\, P(\hat{L}_{BCS}|L_{BCS}) P(I|\hat{L}_{BCS}, z) \quad (10)$$

where Ω is the survey area. In this expression, the first probability $P(L_{BCS}|M)$ is the probability that a cluster of mass M has some intrinsically scattered luminosity L_{BCS} (so is a function of our $L_{CXO}-M_T$ relation parameters A_{LM}, B_{LM}, δ_{LM}). The second probability $P(\hat{L}_{BCS}|L_{BCS})$ is the probability that a cluster of luminosity L_{BCS} would be observed to have a luminosity $\hat{L}_{BCS}$, and so depends on a model of the measurement error on a cluster of arbitrary luminosity. The measurement error is expected to be dominated by counting statistics, but a direct conversion from luminosity to flux to counts would require an exposure time, which is not uniform across the survey. Instead we derived an empirical function to predict the measurement error on a cluster of given flux by fitting a power law to the measurement errors of the (e)BCS fluxes as a function of flux. The best fitting relation had the form

$$\frac{\sigma_F}{F_0} = 0.49 \left(\frac{F_{BCS}}{F_0}\right)^{0.53} \tag{11}$$

with the normalisation factor $F_0 = 10^{-12}$ erg s^{-1} cm^{-2}. The observed scaling is thus very close to the square-root scaling expected for Poisson errors. We also imposed a maximum fractional flux error of 0.4, in line with the (e)BCS catalogues.

The final probability in equation 10, $P(I|\hat{L}_{BCS}, z)$ is the probability that a cluster with an observed BCS luminosity $\hat{L}_{BCS}$ at a redshift z would be included in the subsample. This is a combination of the step function associated with $L_{lim}(z)$, and $P(I|f)$ describing the BCS completeness. Note that in principal, the probability of inclusion should depend on T in addition to $\hat{L}_{BCS}$ and z, since the k-correction for the flux is temperature dependent. However, since the BCS luminosities were estimated from *ROSAT* fluxes without temperature measurements, a reference LT relation was used to provide the temperature for the k-correction. Since our inclusion probability must match as closely as possible the BCS completeness function, we use the same method to k-correct L_{BCS} when estimating f for the selection function (equation 9), which removes the T dependence.

The likelihood of a cluster in our sample having the observed properties $(\hat{L}_{BCS}, \hat{L}_{CXO}, \hat{M})$ is given by

$$\begin{aligned} P(\hat{L}_{BCS}, \hat{L}_{CXO}, \hat{M}, z) = & \int dM \int dL_{BCS} \frac{\phi(M,z)}{\langle N \rangle} \\ & \times P(L_{BCS}|M) P(\hat{L}_{BCS}|L_{BCS}) \\ & \times P(\hat{L}_{CXO}|L_{BCS}) P(\hat{M}|M) \\ & \times P(I|\hat{L}_{BCS}, z). \end{aligned} \tag{12}$$

The quantity $\langle N \rangle$ is the total number of clusters predicted by the model, and is given by the integral of the mass function ϕ over the mass range of interest, and normalises the mass function to a probability distribution for an arbitrary cluster to have a mass M at redshift z. We note that $\langle N \rangle$ is not a parameter of our model, but is a useful parameter to monitor. $P(L_{BCS}|M)$ is as defined above, and the remaining terms are the probability of each of the observables, using the measured uncertainty for that observable. Here we have treated each of the observables as independent, although in principal a covariance will exist between $\hat{L}_{CXO}$ and $\hat{M}$ as the luminosity is determined within an aperture derived from the observed mass. In practice, this effect will be weak as the luminosity is centrally concentrated and is insensitive to the precise choice of aperture. The joint probability of the full set of observed cluster properties is the product of $P(\hat{L}_{BCS}, \hat{L}_{CXO}, \hat{M})$ over all N_{det} observed clusters in the sample. Note that we neglect any observational uncertainty on z.

Mantz et al. (2010b) showed that the final likelihood for the sample of clusters and their observed properties is the product of a Poisson likelihood of N total (detected plus undetected) clusters given the model prediction $\langle N \rangle$, a binomial coefficient accounting for the number of ways of drawing N_{det} detected clusters from the total N, the joint probability of the set of observed cluster properties (the product of equation 12 over the N_{det} clusters) and the probability of not detecting the remaining $N - N_{det}$ clusters. Neglecting terms not dependent on the model parameters, the likelihood simplifies to

$$\mathcal{L}(\hat{L}_{BCS}, \hat{L}_{CXO}, \hat{M}, z) \propto e^{-\langle N_{det} \rangle} \prod_{i=1}^{N_{det}} \langle \tilde{n}_{det,i} \rangle \tag{13}$$

where

$$\langle \tilde{n}_{det,i} \rangle = P(\hat{L}_{BCS}, \hat{L}_{CXO}, \hat{M}) \langle N \rangle \tag{14}$$

for the ith cluster.

Note that our relatively simple selection function $P(I|\hat{L}_{BCS}, z)$ does not depend on any model parameters so can be dropped from equation 12 for the purposes of maximising the likelihood. However, it must be retained in the computation of $\langle N \rangle$ since it is within the integral over $\hat{L}_{BCS}$ – this makes sense, since we expect the selection function to influence the model's prediction of the number of detected clusters.

5.4.2 *Implementation and nuisance parameters*

With the likelihood in equation 13, and priors on the model parameters, we can compute the posterior probability distribution for each parameter using standard Markov Chain Monte Carlo (MCMC) techniques. Our final set of model parameters consists of those parameters describing the $L_{CXO} - M_T$ relation (A_{LM},B_{LM},δ_{LM}), each of which were assigned uniform priors, along with a nuisance parameter described below (naturally marginalised over in the MCMC procedure).

A cross-calibration factor X_{cal} describing the uncertainty in the calibration between *Chandra* and *ROSAT* fluxes was introduced, defined as the ratio of the *Chandra* flux measured within r_{500} to F_{BCS}. This calibration factor thus represents several factors: cross calibration between *ROSAT* and *Chandra* fluxes; a mean aperture correction from r_{500} to the 1.43Mpc radius to which the (e)BCS fluxes were extrapolated; and exclusion of point sources in *Chandra* data that may have been unresolved or only partially excluded in the *ROSAT* data. We can estimate the size of the first two of these contributions to X_{cal} as follows.

M10 found that soft-band *Chandra* luminosities were 14% higher on average than *ROSAT* PSPC fluxes measured in the same aperture (using *Chandra* CALDB version 4.1.2 rather than version 4.3.1 used in our analysis). Meanwhile, if the surface brightness profile of a cluster is approximated by a β-profile (Cavaliere & Fusco-Femiano 1976) with $\beta = 2/3$, then the ratio of the flux enclosed by radius R, F_R, to that

extrapolated to 1.43 Mpc, $F_{1.43Mpc}$ is

$$\frac{F_R}{F_{1.43\mathrm{Mpc}}} = 1 - \left[1 + \left(\frac{R}{r_c}\right)^2\right]^{-1/2} \quad (15)$$

where r_c is the core radius of the profile. Typically $r_c/r_{500} \sim 0.15$ with large scatter (e.g. for the clusters with $M_{500} > 5 \times 10^{15} M_\odot$ in Maughan et al. 2008, the ratio is 0.15 with a log-normal scatter of 90%). This would give a typical aperture correction of 1.06 to scale a flux from r_{500} to 1.43 Mpc.

The value of X_{cal} was estimated from our data, including the low-mass extension of our sample presented in Van der Pyl et al. (in prep.) which comprises *Chandra* observations analysed consistently with those in the current sample. Restricted to clusters well above the selection limit of the samples in order to avoid Eddington bias, they found $X_{cal} = 0.94$, with $\sim 15\%$ scatter. This relatively small factor is compatible with opposing factors of order $10-20\%$ due to the *Chandra*/*ROSAT* cross-calibration and aperture correction largely canceling out. We thus impose a log-normal prior distribution on X_{cal} with mean ln(0.94) and standard deviation 0.15 in natural log space (i.e. a 15% uncertainty).

The analysis also requires a mass function to describe the population distribution, and for this we used the mass function of Tinker et al. (2008). In our analysis we have treated all cosmological parameters as constant, and we take the same approach with the mass function, using a tabulated mass function produced by *HMFcalc* (Murray, Power & Robotham 2013) for our *WMAP*9 cosmology with a virial mass M_{500c} (the mass r_{500} with respect to the critical density of the Universe). We have fixed all cosmological parameters since we are focusing on the scaling relations, and do not expect useful cosmological constraints from our sample. Fixing the cosmological and mass function parameters means that our scaling relations are not marginalised over the uncertainties in those parameters, and should be regarded as estimates for a fixed cosmology (in contrast, the combined cosmology and scaling relation study of Mantz et al. 2010a, does include cosmological and mass function parameters in the analysis).

Our final model thus consists of three parameters describing the LM relation (A_{LM},B_{LM},δ_{LM}), and the nuisance parameter X_{cal} describing the conversion between F_{BCS} and F_{CXO}.

Our fits were performed using the *R* statistical computing environment[4], and the posterior probability distribution was analysed using the Bayesian inference package *Laplace's Demon*[5] within R, which contains many MCMC algorithms. The best fitting model parameters are described by the mean and standard deviation of the posterior probability distribution, as estimated from the MCMC chain after excluding the start of the chain before the parameter values became stationary.

5.4.3 *The L_{CXO}-M_T relation*

The $L_{CXO} - M_T$ relation is plotted in Figure 6, and the best fit parameters are given in Table 5, which include the uncertainty due to that on X_{cal}. The posterior probability distributions of the model parameters and the correlations between parameters are shown in Figure 7. Figure 7 illustrates that the X_{cal} parameter is not degenerate with the parameters of interest.

Figure 6 also shows the best fitting relation of the "all data" sample of M10. This latter relation is derived from a sample of 238 clusters at $z < 0.5$ with *ROSAT* luminosities for all clusters, with *Chandra* follow-up observations providing luminosities and masses estimated from the gas mass, for a subset of 66 objects (39 clusters, including 11 of those observed with *Chandra*, had luminosities and M_{gas} from *ROSAT* PSPC follow-up observations). The M10 LM relation is the most suitable comparison for our work as it is the only other example of a LM relation with full corrections for selection biases. Since the luminosities in M10 were calibrated to a *ROSAT* PSPC reference, to compare with our $L_{CXO} - M_T$ relation, we derived a calibration of the M10 luminosities onto our *Chandra* reference by comparing luminosities for 24 objects in common between the samples. We found a low scatter correlation between the values, with the M10 luminosities higher by a factor of 1.10 on average. This difference is in the opposite sense to that found in M10, where *Chandra* luminosities (using CALDB 4.1.2) were found to be 14% higher than PSPC luminosities. This difference is due to the evolving *Chandra* calibration (we used CALDB 4.6.2), and systematic differences in the analyses. We do not pursue these calibration differences further, but simply scale the M10 LM relation normalisation by a factor 1.10 and note that this difference is typical of cross-calibration uncertainties in X-ray telescope effective areas (Nevalainen, David & Guainazzi 2010). We find the $L_{CXO} - M_T$ relation is not significantly different to the M10 LM relation, with the difference in slope only significant at the 2σ level.

We compare to the BCES fit outlined in Section 5.2, given by the black dashed line in Figure 6. The difference between the two fitting methods is visibly striking, with the normalisation of the fit when accounting for selection effects 2.1 ± 0.4 times lower when not taking into account selection effects (significant at the 3.4σ level). This comparison clearly shows the size of the biases on cluster samples selected to have very luminous clusters, such as the LoCuSS (Zhang et al. 2008) and CCCP (Mahdavi et al. 2013) cluster samples, and is an extreme illustration of the importance of modeling selection biases.

5.4.4 *The $L_{bol} - M_T$ relation*

So far we have been considering the scaling of soft-band luminosity with mass, but it is often useful to refer to the bolometric luminosity L_{bol}. It is not possible to fit our model directly to bolometric luminosities, since the selection function is defined in terms of the soft-band luminosity. Instead we can convert the $L_{CXO} - M_T$ relation to an $L_{bol} - M_T$ relation by using a k-correction.

Using `XSPEC` simulations, we find this k-correction can be approximated by

$$\frac{L_{bol}}{L_{CXO}} = A_k \left(\frac{T}{T_0}\right)^{B_k} \quad (16)$$

with $A_k = 2.08$ and $B_k = 0.54$ for $T_0 = 5$keV, giving

[4] http://www.r-project.org/
[5] http://www.bayesian-inference.com/software

Table 5. Best fitting parameters for the LM relations modeled here. Note that for the M10 method, the L_{BCS}-M_T relation is the plane in which the data were fit. The other relations required mean correction factors to convert them from this plane. The different evolution of the L_{bol}-M_{500} relation is due to the evolving TM relation used to k-correct the soft band luminosities to bolometric luminosities (see §5.4.4). δ_{LM} is the intrinsic scatter measured in natural log space so represents a fractional value.

		$r_{T,500}$			
Relation	Method	A_{LM}	B_{LM}	γ_{LM}	δ_{LM}
L_{CXO}-M_T	BCES	1.21 ± 0.18	1.86 ± 0.36	7/3	0.40 ± 0.07
L_{BCS}-M_T	M10	0.53 ± 0.07	1.77 ± 0.21	7/3	0.52 ± 0.07
L_{CXO}-M_T	M10	0.63 ± 0.08	1.77 ± 0.21	7/3	0.52 ± 0.07
L_{bol}-M_T	M10	1.26 ± 0.16	2.14 ± 0.21	2.69	0.52 ± 0.07

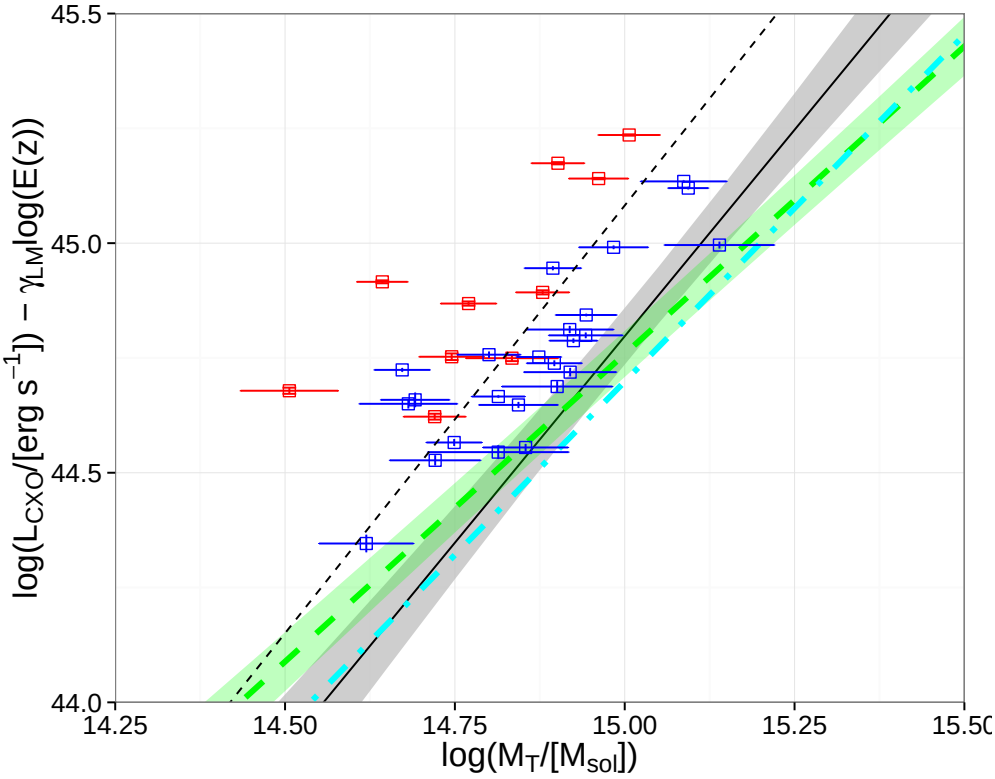

Figure 6. $L_{CXO} - M_T$ relation with best fitting model. The hollow squares show the L_{CXO} luminosities split between the RCC (red) and NRCC (blue) clusters, calibrated to ROSAT reference using the calibration factor X_{cal}. Our best fitting model is shown as the solid black line with the grey shading indicating the 1σ uncertainty. The bold dashed green line and shaded region indicate the best fitting LM relation for the "all data" sample of M10 with its 1σ uncertainty, scaled by a factor of 1.10 to scale the *ROSAT* PSPC luminosties used in M10 onto our *Chandra* reference (see Sect. 5.4.3). The bold cyan dashed-dotted indicates the best fitting LM relation for the BCS only sample of M10 (see Sect. 6.1).

bolometric luminosities accurate to $\lesssim$3% across the range $3 - 15$keV. Combined with a temperature-mass (TM) relation of the form

$$\frac{T}{T_0} = A_{TM} E(z)^{\gamma_{TM}} \left(\frac{M}{M_0}\right)^{B_{TM}} \quad (17)$$

then the bolometric LM relation becomes

$$\begin{aligned} \frac{L_{bol}}{L_0} &= E(z)^{\gamma_{LM}+B_k\gamma_{TM}} A_{LM} A_k A_{TM}^{B_k} \left(\frac{M}{M_0}\right)^{B_{LM}+B_k B_{TM}} \\ &= E(z)^{\gamma_{LM,bol}} A_{LM,bol} \left(\frac{M}{M_0}\right)^{B_{LM,bol}} \quad (18) \end{aligned}$$

Note that the self-similar evolution of the TM relation alters the evolution of the bolometric $L_{bol} - M$ relation from that of the soft-band $L_{CXO} - M_T$ relation.

To derive the $L_{bol} - M_T$ relation, we used the MT relation presented in section 5.1 (note that MT relation was refit in the TM plane for the conversion). The $L_{bol} - M_T$ relation is shown in Figure 8, with the best-fitting model coefficients given in Table 5. The uncertainties on the model parameters include correlated uncertainties on A_{LM}, B_{LM}, and X_{cal} from the posterior chains of the MCMC analysis, and the uncertainty on the slope and normalisation of the TM relation, treating those as independent. This is justified

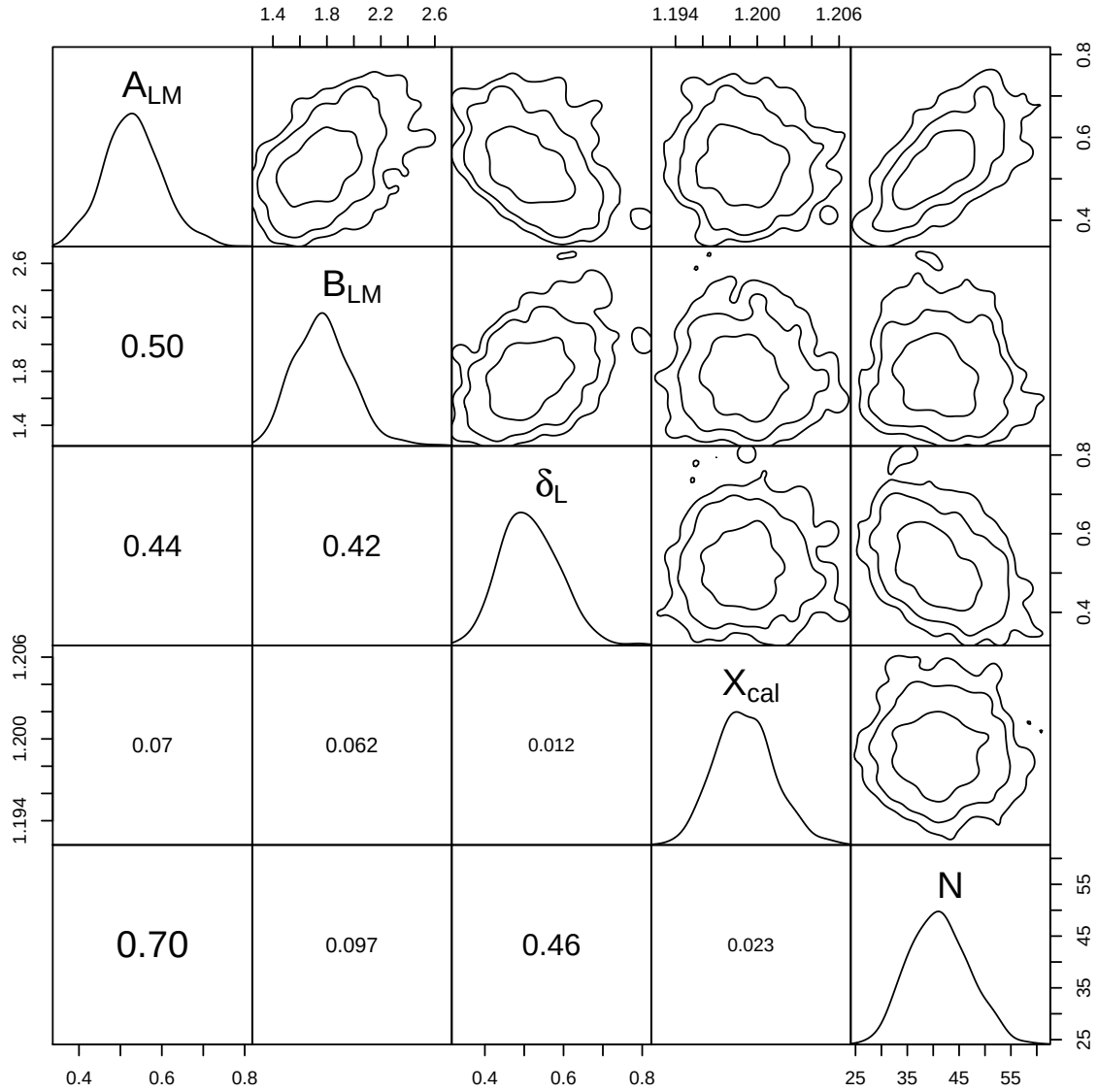

Figure 7. Correlation matrix of the $L_{CXO} - M_T$ relation model. The posterior densities are shown along the diagonal, with 1σ, 2σ, and 3σ confidence contours for the pairs of parameters shown on the upper triangle panels. The lower triangle panels show the Pearson's correlation coefficient for the corresponding pair of parameters (with a text size proportional to the correlation strength).

since there is not a strong covariance between the TM and LM relations (Mantz et al. 2010a; Maughan 2014).

6 DISCUSSION

6.1 Comparison with Mantz et al. (2010b)

We have shown in section 5.4.3 that the derived $L_{CXO} - M_T$ relation is consistent with M10 LM relation. Although consistent, the 2σ difference in slope warrents some discussion since a) the fit method used in this work is based upon M10 work, and b) our sample contains 24 clusters in common with the M10 sample. First, we compare the $L_{CXO} - M_T$ relation to the M10 LM relation using only the BCS cluster sample (M10, private communication).

Figure 6 shows the $L_{CXO} - M_T$ relation, with the bold cyan dashed-dotted line showing the fit from M10 using only the BCS clusters. We find a slightly improved agreement, noting therefore that the difference between our $L_{CXO} - M_T$ and the M10 "all data" relation in Sect. 5.4.3, may be due to our use of only high luminosity (e)BCS clusters. Further differences in the M10 analysis include the use of the gas mass as a proxy for cluster mass and the cosmology is jointly fit in the analysis of the scaling relations. Since our cluster sample is drawn from the tail end of the overall cluster population, the scatter may deviate from a simple log-normal distribution.

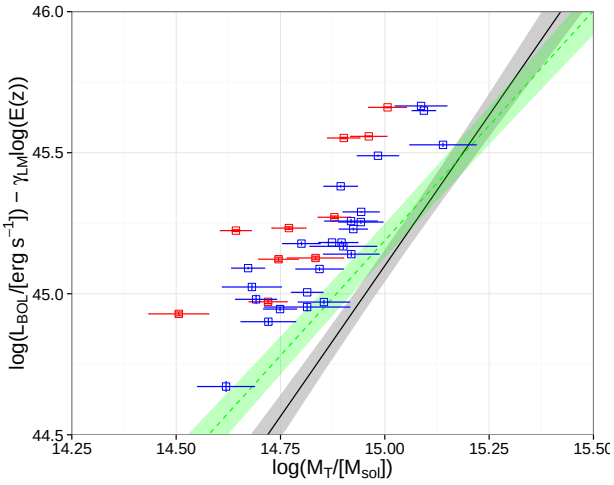

Figure 8. $L_{bol} - M_T$ relation with best fitting model. The hollow squares show the L_{bol} luminosities, split between the RCC (red) and NRCC (blue) clusters, calibrated to ROSAT reference using the calibration factor X_{cal}. Our best fitting model is shown as the solid black line with grey shading indicating the 1σ uncertainty (transformed from the $L_{CXO} - M_T$ using the corrections outlined in Sect. 5.4.4). The dashed green line and shaded region indicate the best fitting bolometric LM relation for the "all data" sample of M10 with its 1σ uncertainty.

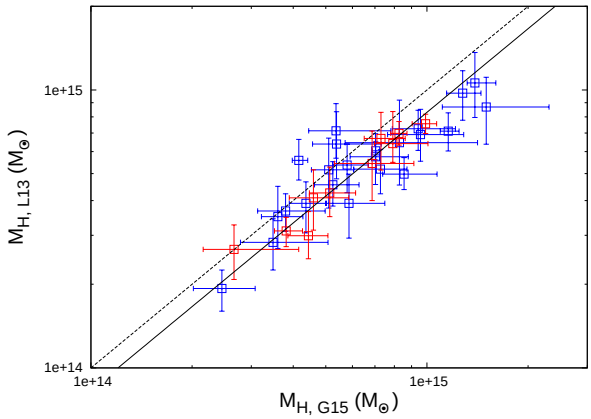

Figure 9. Comparison of the mass estimate determined in this work and those presented in Landry et al. (2013). The dashed line represents a 1:1 relation, with the black line a fit to the data assuming a y=x relation.

6.2 Mass Comparison to Landry et al. (2013)

The sample of clusters presented in this work were also studied in Landry et al. (2013, hereafter L13), the first in this series of papers. We compare here the masses derived in this work to those presented in L13. We note that although this work and L13 use the Vikhlinin et al. (2006) method to derive cluster masses, the implementation was performed separately. There have also been two updates from the L13 paper, to this work. As stated, we use *WMAP*9 cosmology throughout, whereas L13 use *WMAP*7 (Ω_M=0.27, Ω_Λ=0.73 and H_0=70.2, Komatsu et al. 2011). The next change is the versions of CIAO and CALDB used in the separate analysis, we have used CIAO 4.6 and CALDB v4.5.9, whereas L13 use CIAO 4.2 and CALDB v4.3.1.

Figure 9 compares the masses given in L10 to those derived in this work. The black dashed line represents a 1:1 relationship. The black solid line is a fit to the data (using a simple fit of y=x), where we find that our masses are on average 20±3.0% higher than those in L13. We should note that the masses are not compared within the same radii, but within their respective r_{500}. An analysis of our cluster sample with the same cosmology, CIAO and CALDB versions yields a 1:1 mass comparison. Breaking down how the individual contributions of the updated analysis on the sample as a whole is beyond the scope of the current work, however we briefly discuss the effects here. The cosmology will have an effect on the calculated r_{500}, and hence the mass. Changing the cosmology from WMAP7 to WMAP9 changes r_{500} and M_{500} by <1%. Therefore the 20% difference in mass compared to L13 is thought to be due to the different CIAO/CALDB versions. However, understanding the effect of the CALDB on the mass comparison is complicated due to the many different versions of the CALDB released between the L13 analysis and that presented in this work. We further compare our derived masses to those presented in Martino et al. (2014). Martino et al. (2014) studied a sample of 50 clusters from the LoCuSS cluster sample, calculating masses based on *Chandra* observations and utilising temperature profiles to calculate hydrostatic masses. Using 21 clusters in common between the LoCuSS sample and the clusters in this work, we find a 1:1 agreement (using a y=x fit).

6.3 Systematic Effects

Throughout this paper we have assumed a *WMAP*9 cosmology, however, recently data from *Planck* finds a different cosmology (Planck Collaboration et al. 2015). Although the difference is not statistically significant, the change in cosmology can effect our results, since we do not include errors on the cosmological parameters and consider them fixed in our analysis. We discuss here, qualitatively, how the updated cosmology might impact our results. As stated in the previous section, the effect of changing the cosmology is negligible on the derived cluster properties when changing from *WMAP*7 to *WMAP*9. Although the change is larger for the *Planck* cosmology, the derived properties will change only at the 1% level. Therefore, the observed LM relation will remain largely unchanged. The cosmology will also impact the bias-correction fitting of the $L_{CXO} - M_T$. The *Planck* cosmology currently predicts a higher value of σ_8 (the fluctuation amplitude at 8 h^{-1} Mpc) compared to *WMAP*9. This would lead to an increased number of clusters predicted by our model. Due to the strong positive correlation of the normalisation of the LM relation with the predicted number of clusters (see Fig 7), an increase in the number of clusters would increase the normalisation of the LM relation. Therefore, the fit to the observed clusters would be improved. We should note however that the current number of predicted clusters by our best fitting model is 38, a good agreement with the number of clusters in our sample. Although the fit to the $L_{CXO} - M_T$ may be improved if using the *Planck* cosmology, an increase in the number of clusters predicted

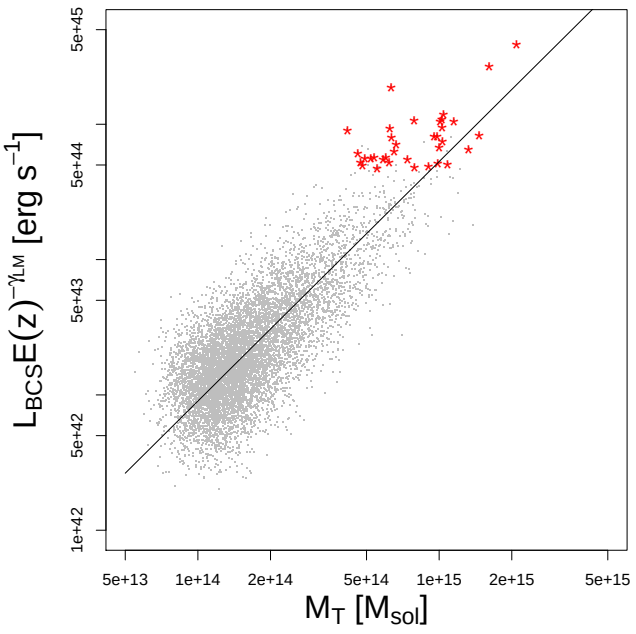

Figure 10. Simulated clusters (grey points) based on the best-fitting $L_{CXO} - M_T$ relation (black line), with the red stars highlighting the clusters selected when applying the selection function outlined in Sect. 5.3.

may indicate that the fit would not be a good description of the data.

We stated in Section 6.1 that the assumption of a log-normal distribution may not be appropriate for our cluster sample due to the high luminosity selection of our cluster sample. M10 explored this assumption and found no evidence for asymmetry in the LM relation scatter. However, this assumption may not hold true for our highly biased sample. We illustrate this point in Figure 10, which shows a set of simulated clusters (grey points) based on the best-fitting $L_{CXO} - M_T$ relation (black line). If our selection function outlined in Section 5.3 is applied to the simulated clusters, then the clusters selected are given by the red stars. This clearly outlines the selection biases involved when selecting clusters based on a high luminosity cut, and shows that a log-normal scatter may not be appropriate for these clusters.

Throughout the analysis of the $L_{CXO} - M_T$ we have used the masses calculated via the $M_H - T$ relation (see Sect. 5.1). We discuss here the effect of using purely hydrostatic mass estimates on the LM relation (denoted $L_{CXO} - M_H$ relation when using hydrostatic masses). Full results of the $L_{CXO} - M_H$ relation is presented in Appendix B, with the $L_{CXO} - M_H$ relation shown in Figure B1. We find that the normalisation of the $L_{CXO} - M_H$ is fully consistent with the $L_{CXO} - M_T$, however the slope appears somewhat shallower. Although this is the case, the discrepancy is only significant at the 1.8σ level. However, we can understand the change in slope of the $L_{CXO} - M_H$ via the dependence of the slope of the LM relation on the slope of the TM relation (B_{TM}). From Maughan (2014) we can write the slope of the LM relation as

$$B_{LM} = 2B_{\mu M} + \frac{1}{2}B_{TM} + B_{QM} - 2 \quad (19)$$

where $B_{\mu M}$ is the slope of the gas mass - total mass relation. B_{TM} is the recipricol of B_{MT}, therefore, the shallower slope of the $L_{CXO} - M_H$ can be fully explained by the shallower slope of the $M_H - T$ relation of the RCC clusters compared to the NRCC clusters.

7 SUMMARY AND CONCLUSIONS

Using a statistically complete sample of 34 galaxy clusters we have derived the X-ray properties of the cluster sample, and constructed scaling relations between these properties and the cluster mass. Our main conclusions are as follows.

(i) Using the central cooling time, the cuspiness of the gas density profile, and the centroid shift, we separate the cluster sample into relaxed cool core (RCC) and non-cool core (NRCC) clusters. We find 10/34 RCC clusters and 24/34 NRCC clusters.

(ii) We derive hydrostatic mass estimates for the cluster sample utilising gas density and temperature profiles.

(iii) Deriving the scaling relation between the temperature and mass for the RCC sample, we find a slope of A_{MT}=1.39±0.14, consistent with the self-similar expectation (i.e. A_{TM}=1.5). Using this MT relation, we derive the masses of the whole cluster sample.

(iv) Taking fully into account selection effects, we fit for the luminosity-mass relation, finding a slope of B_{LM}=1.80±0.24 and scatter δ_{LM}=0.62±0.10.

We have studied a highly biased cluster sample, where the selection has a profound effect on the derived scaling relations. We have shown the importance of taking into account the selection effects when fitting for the observed scaling relations. This is crucial for the understanding of scaling laws of cluster samples when used for the purposes of cosmology. Current and upcoming cluster surveys (e.g. *XXL*, *Planck*, clusters detected with *e-ROSITA*) will all require a method of determining the cluster mass for cosmological studies. This will most likely come in the form of a mass-observable scaling relation, for which the selection effects will need to be fully accounted for.

ACKNOWLEDGMENTS

PG acknowledges support from the UK Science and Technology Facilities Council. We thank A. Mantz for useful discussions and for providing additional fits used in the comparison to his work.

REFERENCES

Akritas M. G., Bershady M. A., 1996, ApJ, 470, 706
Allen S. W., Evrard A. E., Mantz A. B., 2011, ARA&A, 49, 409
Allen S. W., Rapetti D. A., Schmidt R. W., Ebeling H., Morris R. G., Fabian A. C., 2008, MNRAS, 383, 879
Andreon, S. 2012, A&A, 546, A6
Arnaud, K. A. 1996, Astronomical Data Analysis Software and Systems V, 101, 17

Arnaud M., Evrard A. E., 1999, MNRAS, 305, 631
Arnaud M., Pointecouteau E., Pratt G. W., 2005, A&A, 441, 893
—, 2007, A&A, 474, L37
Bauer F. E., Fabian A. C., Sanders J. S., Allen S. W., Johnstone R. M., 2005, MNRAS, 359, 1481
Bharadwaj, V., Reiprich, T. H., Lovisari, L., & Eckmiller, H. J. 2015, A&A, 573, A75
Böhringer H. et al., 2000, ApJS, 129, 435
Cavaliere A., Fusco-Femiano R., 1976, A&A, 49, 137
Comis B., de Petris M., Conte A., Lamagna L., de Gregori S., 2011, MNRAS, 418, 1089
Dahle H., 2006, ApJ, 653, 954
Dahle H., Kaiser N., Irgens R. J., Lilje P. B., Maddox S. J., 2002, ApJS, 139, 313
Ebeling H., Edge A. C., Allen S. W., Crawford C. S., Fabian A. C., Huchra J. P., 2000, MNRAS, 318, 333
Ebeling H., Edge A. C., Bohringer H., Allen S. W., Crawford C. S., Fabian A. C., Voges W., Huchra J. P., 1998, MNRAS, 301, 881
Eke V. R., Cole S., Frenk C. S., Patrick Henry J., 1998, MNRAS, 298, 1145
Evans I. N. et al., 2010, ApJS, 189, 37
Giles P. A., Maughan B. J., Birkinshaw M., Worrall D. M., Lancaster K., 2012, MNRAS, 419, 503
Hao J. et al., 2010, ApJS, 191, 254
Henry J. P., 1997, ApJ, 489, L1+
Henry J. P., Arnaud K. A., 1991, ApJ, 372, 410
Hinshaw G. et al., 2013, ApJS, 208, 19
Hoekstra H., 2007, MNRAS, 379, 317
Hudson D. S., Mittal R., Reiprich T. H., Nulsen P. E. J., Andernach H., Sarazin C. L., 2010, A&A, 513, A37
Jenkins A., Frenk C. S., White S. D. M., Colberg J. M., Cole S., Evrard A. E., Couchman H. M. P., Yoshida N., 2001, MNRAS, 321, 372
Kaiser, N. 1986, MNRAS, 222, 323
Kalberla P. M. W., Burton W. B., Hartmann D., Arnal E. M., Bajaja E., Morras R., Pöppel W. G. L., 2005, A&A, 440, 775
Kravtsov A. V., Vikhlinin A., Nagai D., 2006, ApJ, 650, 128
Komatsu, E., Smith, K. M., Dunkley, J., et al. 2011, ApJS, 192, 18
Landry, D., Bonamente, M., Giles, P., et al. 2013, MNRAS, 433, 2790
Lopes P. A. A., de Carvalho R. R., Gal R. R., Djorgovski S. G., Odewahn S. C., Mahabal A. A., Brunner R. J., 2004, AJ, 128, 1017
Lovisari, L., Reiprich, T. H., & Schellenberger, G. 2015, A&A, 573, A118
Mahdavi A., Hoekstra H., Babul A., Henry J. P., 2008, MNRAS, 384, 1567
Mantz A., Allen S. W., Ebeling H., Rapetti D., 2008, MNRAS, 387, 1179
Mahdavi, A., Hoekstra, H., Babul, A., et al. 2013, ApJ, 767, 116
Mantz A., Allen S. W., Ebeling H., Rapetti D., Drlica-Wagner A., 2010a, MNRAS, 406, 1773
Mantz A., Allen S. W., Rapetti D., Ebeling H., 2010b, MNRAS, 406, 1759
Markevitch M., 1998, ApJ, 504, 27
Markevitch M. et al., 2003, ApJ, 583, 70
Martino, R., Mazzotta, P., Bourdin, H., et al. 2014, MNRAS, 443, 2342
Maughan B. J., 2014, MNRAS, 437, 1171
Maughan B. J., Giles P. A., Randall S. W., Jones C., Forman W. R., 2012, MNRAS, 421, 1583
Maughan B. J., Jones C., Forman W., Van Speybroeck L., 2008, ApJS, 174, 117
Meneghetti M., Rasia E., Merten J., Bellagamba F., Ettori S., Mazzotta P., Dolag K., Marri S., 2010, A&A, 514, A93
Mitchell R. J., Ives J. C., Culhane J. L., 1977, MNRAS, 181, 25P
Mittal R., Hicks A., Reiprich T. H., Jaritz V., 2011, A&A, 532, A133
Murray S., Power C., Robotham A., 2013, ArXiv e-prints
Nagai D., Kravtsov A. V., Vikhlinin A., 2007, ApJ, 668, 1
Navarro J. F., Frenk C. S., White S. D. M., 1997, ApJ, 490, 493
Nevalainen J., David L., Guainazzi M., 2010, A&A, 523, A22
O'Hara T. B., Mohr J. J., Bialek J. J., Evrard A. E., 2006, ApJ, 639, 64
Planck Collaboration, Ade, P. A. R., Aghanim, N., et al. 2015, arXiv:1502.01589
Poole G. B., Fardal M. A., Babul A., McCarthy I. G., Quinn T., Wadsley J., 2006, MNRAS, 373, 881
Pratt G. W., Croston J. H., Arnaud M., Böhringer H., 2009, A&A, 498, 361
Reiprich T. H., Böhringer H., 2002, ApJ, 567, 716
Romer, A. K., Viana, P. T. P., Liddle, A. R., & Mann, R. G. 2001, ApJ, 547, 594
Santos J. S., Tozzi P., Rosati P., Böhringer H., 2010, A&A, 521, A64
Sarazin C. L., 1988, X-ray emission from clusters of galaxies, Sarazin, C. L., ed.
Smith R. K., Brickhouse N. S., Liedahl D. A., Raymond J. C., 2001, ApJ, 556, L91
Tinker J., Kravtsov A. V., Klypin A., Abazajian K., Warren M., Yepes G., Gottlöber S., Holz D. E., 2008, ApJ, 688, 709
Vikhlinin A., Burenin R., Forman W. R., Jones C., Hornstrup A., Murray S. S., Quintana H., 2007, in Heating versus Cooling in Galaxies and Clusters of Galaxies, H. Böhringer, G. W. Pratt, A. Finoguenov, & P. Schuecker , ed., p. 48
Vikhlinin A. et al., 2009a, ApJ, 692, 1033
Vikhlinin A., Kravtsov A., Forman W., Jones C., Markevitch M., Murray S. S., Van Speybroeck L., 2006, ApJ, 640, 691
Vikhlinin A. et al., 2009b, ApJ, 692, 1060
Wang Q. D., Ulmer M. P., Lavery R. J., 1997, MNRAS, 288, 702
Wright C. O., Brainerd T. G., 2000, ApJ, 534, 34
Zhang, Y.-Y., Finoguenov, A., Böhringer, H., et al. 2008, A&A, 482, 451
Zhang Y.-Y. et al., 2010, ApJ, 711, 1033

APPENDIX A: PARAMETERS OF THE GAS DENSITY AND TEMPERATURE PROFILES

Here we give the parameters of the gas density and temperature profiles of the cluster sample. Tables A1 and A2 lists the individual parameters of the fits to the gas density and temperature profiles respectively.

APPENDIX B: THE HYDROSTATIC LUMINOSITY-MASS RELATION

In this paper we have presented the LM relation for our sample, for the properties derived within an r_{500} calculated from the RCC MT relation (see § 5.1). Here we present the LM relations using hydrostatic masses for all clusters, and the luminosities derived within the hydrostatic r_{500} ($\mathrm{r_{H,500}}$). Table B1 lists the properties of the clusters within $\mathrm{r_{H,500}}$. The L_{CXO}-M_{500} relation using hydrostatic masses is plotted in Figure B1, and the best fit paramteres are given in Table B2.

Table A1. Table listing the individual parameters of the fit to the gas density profile for each of the clusters in our sample.

Cluster	n_0 10^{-3} cm^{-3}	r_c (kpc)	r_s (kpc)	α	β	ϵ
A2204†	24.579	67.778	1363.850	2.028	0.532	3.095
RXJ1720.1+2638†	36.927	47.171	695.129	0.781	0.542	1.088
A586	16.085	51.421	161.327	0.001	0.323	1.837
A1914	14.004	154.980	2703.460	0.000	0.718	5.000
A665	11.249	67.700	1367.420	0.000	0.397	5.000
A115	29.314	29.186	3967.680	0.668	0.445	5.000
A520	3.408	391.718	339.217	0.000	0.685	0.760
A963	10.907	96.634	997.588	0.898	0.518	3.384
A1423†	20.548	39.845	1632.000	0.330	0.446	3.257
A773	8.315	138.667	846.138	0.000	0.552	1.365
A1763	7.557	133.460	1351.600	0.000	0.500	2.582
A2261	13.171	114.317	2382.670	0.922	0.587	1.629
A1682	2.593	278.998	3046.010	0.757	0.610	0.000
A2111	4.753	190.063	1061.220	0.161	0.602	0.000
Z5247	0.954	396.838	1905.930	1.051	0.423	5.000
A267	9.892	134.225	3333.110	0.000	0.655	0.106
A2219	5.995	216.035	331.133	0.507	0.300	2.250
A2390	68.229	18.435	579.989	0.000	0.368	2.878
Z2089†	18.299	71.553	142.615	1.751	0.628	0.000
RXJ2129.6+0005†	9.959	116.326	1760.560	1.800	0.566	5.000
A1835†	100.000	27.147	469.409	0.368	0.483	1.531
A68	5.240	259.711	665.144	0.416	0.783	0.000
MS1455.0+2232†	13.548	106.649	100.000	1.865	0.411	1.412
A2631	3.634	370.272	2472.830	0.453	0.819	0.000
A1758	2.903	798.833	399.279	0.000	0.300	3.855
A1576	10.987	89.185	1191.130	0.000	0.501	1.913
A697	8.734	170.861	923.611	0.000	0.548	1.609
RXJ0439.0+0715†	1.483	799.982	200.646	1.552	0.701	1.641
RXJ0437.1+0043†	44.707	20.610	198.695	0.000	0.353	1.558
A611	2.274	735.655	130.495	1.353	0.433	1.886
Z7215	5.550	190.280	1148.840	0.000	0.647	0.000
Z3146†	11.306	163.032	3984.170	1.866	0.705	0.000
A781	2.684	466.725	234.173	0.000	0.403	1.674
A2552	8.841	88.866	244.596	0.837	0.300	1.778

APPENDIX C: IMAGES, GAS DENSITY AND TEMPERATURE PROFILES

Here we show images, gas density and temperature profiles for our cluster sample. Figure C1 shows an adaptively smoothed image of the cluster measuring 3×3 Mpc on a side (left), the emmisivity profile with the best fitting gas density profile (middle) and the temperature profile (right) with the best fitting three dimentional model (red) and the corresponding projected profile (blue) for the cluster A2204. Figures C2-C33 show the rest of the cluster sample.

This paper has been typeset from a TEX/LATEX file prepared by the author.

Table A2. Table listing the individual parameters of the fit to the temperature profile for each of the clusters in our sample. † indicates RCC clusters.

Cluster	T_0 (keV)	r_{cool} (kpc)	T_{min} (keV)	r_t (kpc)	a_{cool}	a	b	c
A2204†	13.874	26.919	5.719	1231.11	3.157	-0.164	3.414	6.165
RXJ1720.1+2638†	11.855	93.095	5.458	275.171	0.074	-0.287	5.000	0.416
A586	11.162	41.308	5.999	499.848	0.613	-0.061	1.096	0.916
A1914	16.434	22.725	4.803	240.319	0.483	0.199	0.592	0.204
A665	16.035	17.916	0.100	500.000	0.209	-0.118	1.913	0.450
A115	10.540	156.385	2.220	100.000	2.302	0.170	1.471	0.000
A520	12.752	42.111	4.110	500.000	0.212	-0.083	4.880	0.755
A963	16.372	178.655	0.100	379.167	0.001	-0.082	5.000	0.955
A1423†	17.696	487.570	3.455	499.685	0.827	-0.025	1.491	1.000
A773	12.252	41.849	2.536	217.694	0.390	0.165	1.602	0.000
A1763	13.040	23.973	4.118	291.134	0.001	-0.009	3.715	0.000
A2261	13.741	38.831	5.995	462.556	0.302	-0.131	3.418	1.000
A1682	13.487	79.119	0.100	185.898	2.420	0.482	0.004	0.002
A2111	12.531	26.204	6.000	499.999	0.003	-0.206	3.279	0.846
Z5247	8.740	10.001	5.083	102.239	3.000	0.293	0.377	0.006
A267	6.717	60.828	4.545	499.999	0.206	0.060	4.999	0.595
A2219	23.178	207.191	1.447	499.990	0.000	-0.024	1.963	0.217
A2390	12.014	47.379	3.083	248.913	1.032	-0.135	1.467	0.248
Z2089†	6.540	77.635	2.691	106.135	2.922	0.089	0.396	0.103
RXJ2129.6+0005†	13.644	79.691	0.865	409.636	0.391	-0.101	5.000	0.997
A1835†	13.668	64.655	0.100	924.648	0.744	-0.007	4.025	1.878
A68	17.551	28.986	2.469	226.487	0.330	0.221	0.827	0.181
MS1455.0+2232†	6.086	10.000	3.466	353.861	2.328	-0.113	5.000	0.347
A2631	15.608	52.538	0.401	155.199	3.000	0.097	0.509	0.281
A1758	8.603	53.701	5.597	280.765	0.656	-0.241	1.343	0.080
A1576	11.735	19.588	1.407	229.401	2.012	-0.102	1.578	0.505
A697	6.717	60.828	4.545	499.999	0.206	0.060	4.999	0.595
RXJ0439.0+0715†	9.802	89.365	2.354	500.000	0.417	0.073	7.382	1.029
RXJ0437.1+0043†	10.666	21.516	0.111	828.236	0.416	-0.072	10.000	2.000
A611	8.105	26.170	0.100	470.611	3.000	0.056	5.000	0.484
Z7215	23.001	343.972	5.979	420.755	2.868	0.200	0.932	1.000
Z3146†	10.373	21.860	4.890	500.000	1.245	-0.212	4.930	0.804
A781	12.471	10.000	3.053	499.999	0.306	-0.150	1.887	0.919
A2552	19.446	425.345	4.868	487.073	1.749	0.226	1.195	0.598

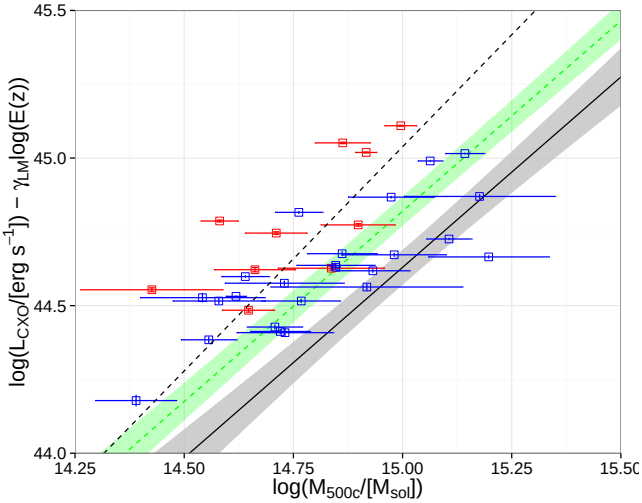

Figure B1. L_{CXO}-M_H relation with best fitting model. The masses here are based on hydrostatic mass estimates. The hollow squares show the L_{CXO} luminosities. Our best fitting model is shown as the solid black line with grey shading indicating the 1σ uncertainty. The dashed green line and shaded region indicate the best fitting LM relation for the "all data" sample of M10 with its 1σ uncertainty. The normalisation of the M10 relation has been reduced by 10% to account for cross-calibration of luminosities between *ROSAT* PSPC and *Chandra* as described in the text.

[h]

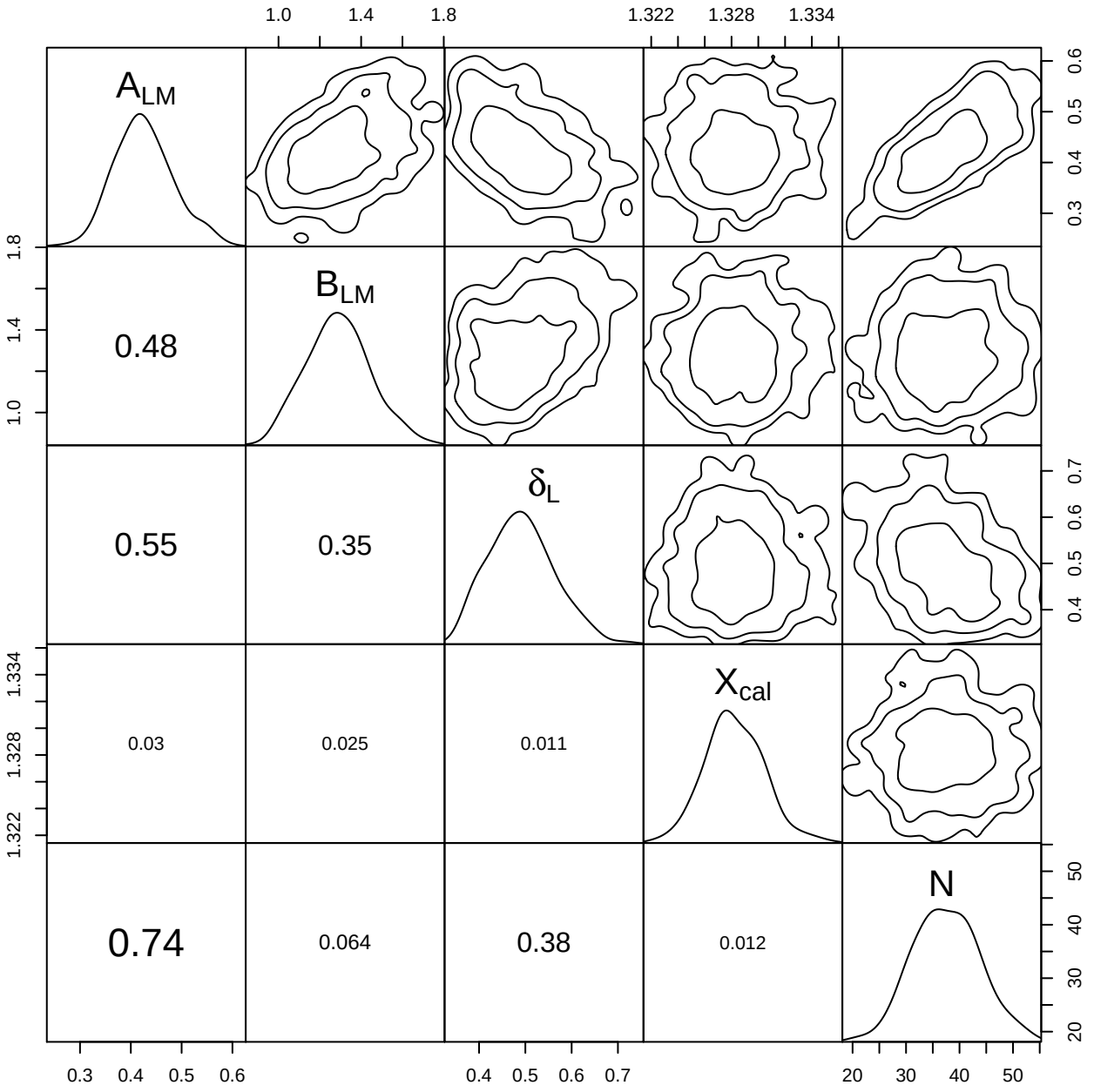

Figure B2. Correlation matrix of the *LM* relation model. The posterior densities are shown along the diagonal, with 1σ, 2σ, and 3σ confidence contours for the pairs of parameters shown on the upper triangle panels. The lower triangle panels show the Pearson's correlation coefficient for the corresponding pair of parameters (with a text size proportional to the correlation strength).

Table B1. X-ray properties of our cluster sample within r_{500}s determined from the hydrostatic mass analysis (see §3.4). † Indicates RCC clusters.

Hydrostatic					
Cluster	$r_{H,500}$ (Mpc)	$L_{H,bcs}$ (10^{44} ergs s^{-1})	$L_{H,bol}$ (10^{44} ergs s^{-1})	T_H (keV)	M_H ($10^{14}M_\odot$)
A2204†	$1.36^{+0.03}_{-0.03}$	16.25±0.06	42.44±0.14	$9.23^{+0.41}_{-0.42}$	$8.25^{+0.47}_{-0.45}$
RXJ1720.1+2638†	$1.34^{+0.11}_{-0.05}$	9.44±0.10	22.53±0.23	$8.01^{+0.39}_{-0.39}$	$7.91^{+2.16}_{-0.93}$
A586	$1.05^{+0.10}_{-0.06}$	5.21±0.12	12.42±0.28	$6.02^{+0.59}_{-0.59}$	$3.80^{+1.18}_{-0.66}$
A1914	$1.42^{+0.13}_{-0.08}$	11.72±0.11	36.87±0.34	$9.37^{+0.57}_{-0.57}$	$9.41^{+2.75}_{-1.53}$
A665	$1.56^{+0.07}_{-0.06}$	8.45±0.06	23.68±0.16	$8.81^{+0.60}_{-0.44}$	$12.78^{+1.70}_{-1.34}$
A115	$1.07^{+0.02}_{-0.02}$	5.52±0.03	12.03±0.07	$7.21^{+0.31}_{-0.35}$	$4.15^{+0.26}_{-0.18}$
A520	$1.27^{+0.01}_{-0.01}$	6.93±0.03	18.64±0.09	$7.91^{+0.26}_{-0.27}$	$7.04^{+0.21}_{-0.16}$
A963	$1.08^{+0.05}_{-0.04}$	6.58±0.06	15.35±0.15	$5.77^{+0.31}_{-0.32}$	$4.36^{+0.63}_{-0.47}$
A1423†	$1.09^{+0.05}_{-0.05}$	5.06±0.07	11.39±0.17	$6.26^{+0.39}_{-0.39}$	$4.44^{+0.63}_{-0.58}$
A773	$1.35^{+0.11}_{-0.06}$	6.89±0.10	19.01±0.28	$8.15^{+0.42}_{-0.42}$	$8.55^{+2.17}_{-1.17}$
A1763	$1.40^{+0.14}_{-0.10}$	7.97±0.11	22.68±0.33	$8.82^{+0.74}_{-0.54}$	$9.57^{+3.30}_{-1.93}$
A2261	$1.18^{+0.06}_{-0.04}$	11.09±0.12	30.28±0.32	$8.07^{+0.40}_{-0.40}$	$5.79^{+0.91}_{-0.55}$
A1682	$1.01^{+0.06}_{-0.04}$	4.10±0.10	9.70±0.25	$6.70^{+0.76}_{-0.55}$	$3.60^{+0.67}_{-0.38}$
A2111	$1.14^{+0.07}_{-0.05}$	4.38±0.07	11.31±0.19	$7.62^{+0.63}_{-0.63}$	$5.25^{+1.03}_{-0.62}$
Z5247	$0.89^{+0.07}_{-0.06}$	2.56±0.11	5.33±0.23	$5.09^{+0.55}_{-0.52}$	$2.45^{+0.63}_{-0.44}$
A267	$1.00^{+0.13}_{-0.07}$	5.70±0.20	12.07±0.43	$4.99^{+0.44}_{-0.44}$	$3.48^{+1.59}_{-0.70}$
A2219	$1.49^{+0.04}_{-0.03}$	16.56±0.11	56.19±0.37	$11.53^{+0.48}_{-0.49}$	$11.57^{+0.89}_{-0.61}$
A2390	$1.58^{+0.08}_{-0.03}$	17.55±0.09	59.24±0.31	$11.38^{+0.75}_{-0.94}$	$13.89^{+2.14}_{-0.72}$
Z2089†	$0.91^{+0.15}_{-0.06}$	6.06±0.09	10.79±0.16	$4.41^{+0.46}_{-0.36}$	$2.67^{+1.49}_{-0.51}$
RXJ2129.6+0005†	$1.13^{+0.07}_{-0.05}$	9.44±0.10	21.91±0.23	$6.79^{+0.47}_{-0.35}$	$5.14^{+0.99}_{-0.67}$
A1835†	$1.40^{+0.04}_{-0.04}$	22.26±0.07	59.31±0.19	$9.85^{+0.41}_{-0.42}$	$9.91^{+0.78}_{-0.87}$
A68	$1.32^{+0.25}_{-0.15}$	6.33±0.17	19.22±0.52	$8.31^{+1.15}_{-1.00}$	$8.28^{+5.86}_{-2.57}$
MS1455.0+2232†	$1.02^{+0.04}_{-0.03}$	10.81±0.08	21.90±0.16	$5.38^{+0.28}_{-0.21}$	$3.81^{+0.45}_{-0.29}$
A2631	$1.24^{+0.10}_{-0.07}$	7.81±0.13	20.61±0.33	$7.02^{+0.57}_{-0.39}$	$7.03^{+1.77}_{-1.12}$
A1758	$1.62^{+0.21}_{-0.10}$	8.51±0.10	23.62±0.28	$8.82^{+0.45}_{-0.33}$	$15.75^{+7.22}_{-2.80}$
A1576	$1.17^{+0.10}_{-0.06}$	5.91±0.09	16.52±0.24	$7.81^{+0.61}_{-0.61}$	$5.86^{+1.63}_{-0.84}$
A697	$1.59^{+0.24}_{-0.15}$	13.36±0.23	45.66±0.79	$12.58^{+1.32}_{-1.24}$	$15.01^{+8.07}_{-3.90}$
RXJ0439.0+0715†	$1.09^{+0.09}_{-0.06}$	7.09±0.11	16.70±0.27	$6.42^{+0.42}_{-0.42}$	$4.59^{+1.26}_{-0.70}$
RXJ0437.1+0043†	$1.23^{+0.12}_{-0.10}$	7.63±0.11	18.16±0.27	$7.44^{+0.78}_{-0.79}$	$6.87^{+2.28}_{-1.56}$
A611	$1.13^{+0.15}_{-0.07}$	6.79±0.13	19.15±0.37	$8.47^{+0.97}_{-0.75}$	$5.36^{+0.45}_{-0.92}$
Z7215	$1.13^{+0.12}_{-0.06}$	4.62±0.15	11.80±0.39	$6.98^{+1.13}_{-0.92}$	$5.38^{+1.93}_{-0.81}$
Z3146†	$1.25^{+0.07}_{-0.05}$	20.29±0.11	48.42±0.26	$8.27^{+0.36}_{-0.36}$	$7.30^{+1.32}_{-0.79}$
A781	$1.11^{+0.06}_{-0.04}$	4.92±0.08	12.07±0.21	$6.57^{+0.41}_{-0.36}$	$5.10^{+0.95}_{-0.57}$
A2552	$1.24^{+0.08}_{-0.07}$	8.73±0.16	24.35±0.43	$8.32^{+0.76}_{-0.68}$	$7.27^{+1.45}_{-1.22}$

Table B2. Best fitting parameters for the LM relations modelled here. Note that L_{BCS}-M_H is the plane in which the data were fit. The other relations required mean correction factors to convert them from this plane. The different evolution of the L_{bol}-M_{500} relation is due to the evolving TM relation used to k-correct the soft band luminosities to bolometric luminosities (see Sect. 5.4.4). δ_{LM} is the intrinsic scatter measured in natural log space so represents a fractional value.

Relation	Method	$r_{H,500}$ A_{LM}	B_{LM}	γ_{LM}	δ_{LM}
L_{CXO}-M_H	BCES	1.07 ± 0.13	1.23 ± 0.24	7/3	0.38 ± 0.05
L_{BCS}-M_H	M10	0.43 ± 0.06	1.29 ± 0.15	7/3	0.49 ± 0.07
L_{CXO}-M_H	M10	0.57 ± 0.08	1.29 ± 0.15	7/3	0.49 ± 0.07
L_{bol}-M_H	M10	1.12 ± 0.15	1.59 ± 0.15	2.69	0.49 ± 0.07

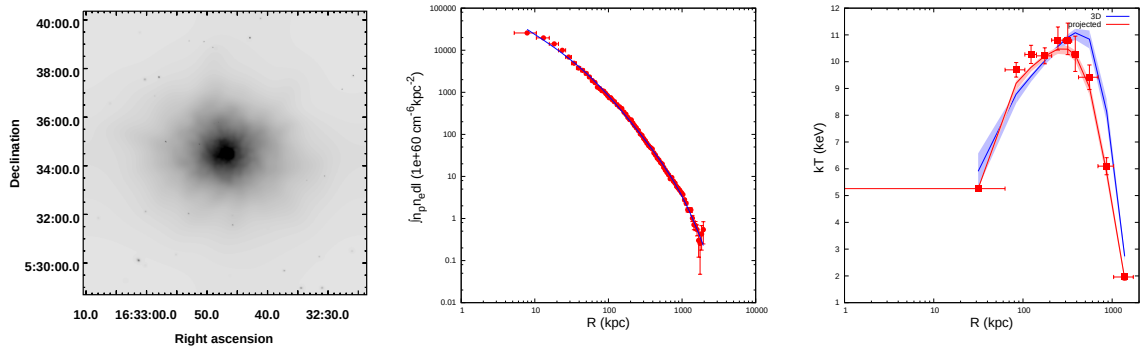

Figure C1. Left: An adaptively smoothed image of the cluster A2204 (3×3 Mpc on a side); Center: Observed projected emissivity profile for A2204, with the best fitting gas density profile shown by the solid blue line; Right: Temperature profile for A2204. The solid red line shows the best fitting three dimentional model to the temperature profile, and the solid blue line represents the corresponding projected profile. The red and blue shaded regions show the corresponding uncertainties on the three dimentional model and projected profile respectively,and obtained from Monte Carlo simulations.

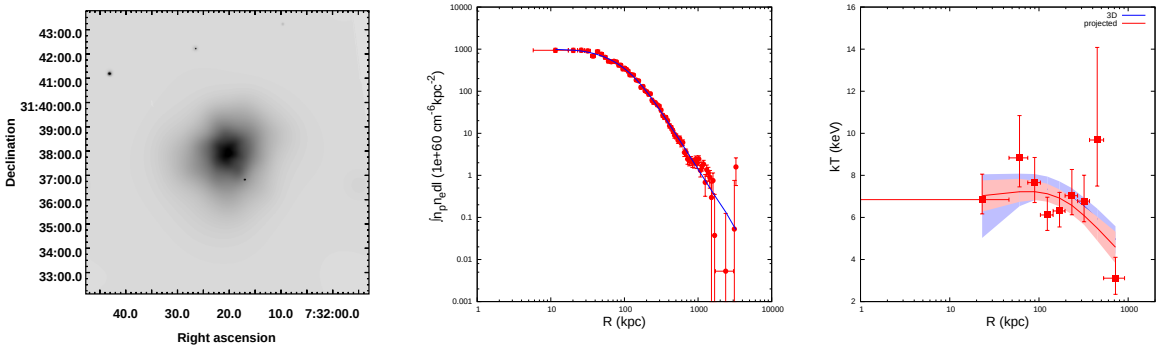

Figure C2. Same as Figure C1 but for A586.

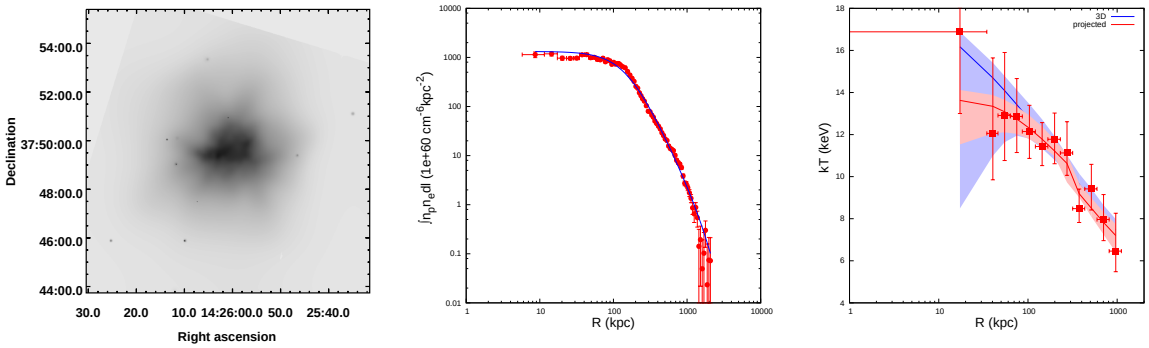

Figure C3. Same as Figure C1 but for A1914.

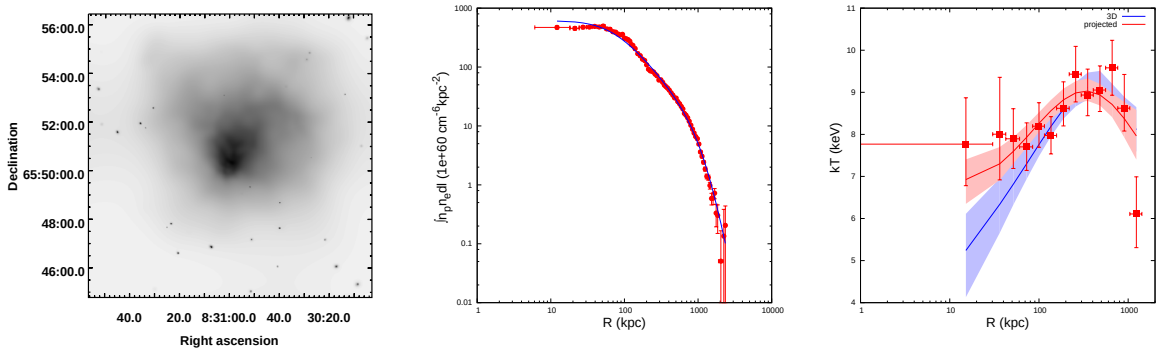

Figure C4. Same as Figure C1 but for A665.

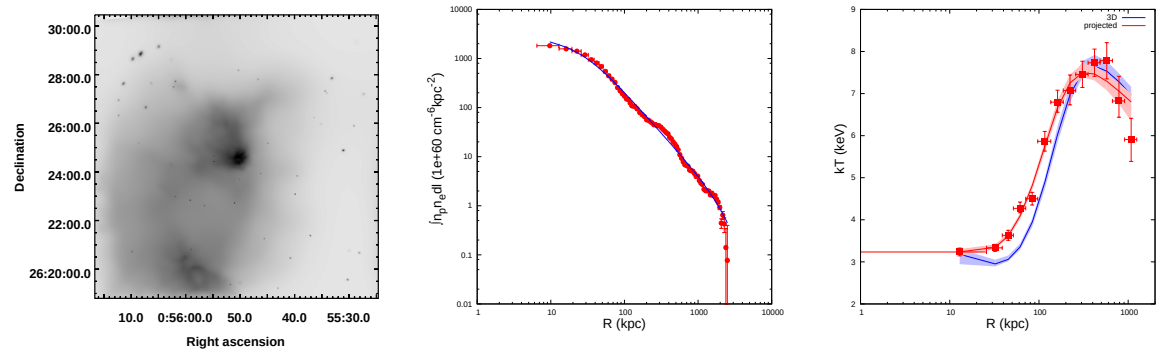

Figure C5. Same as Figure C1 but for A115.

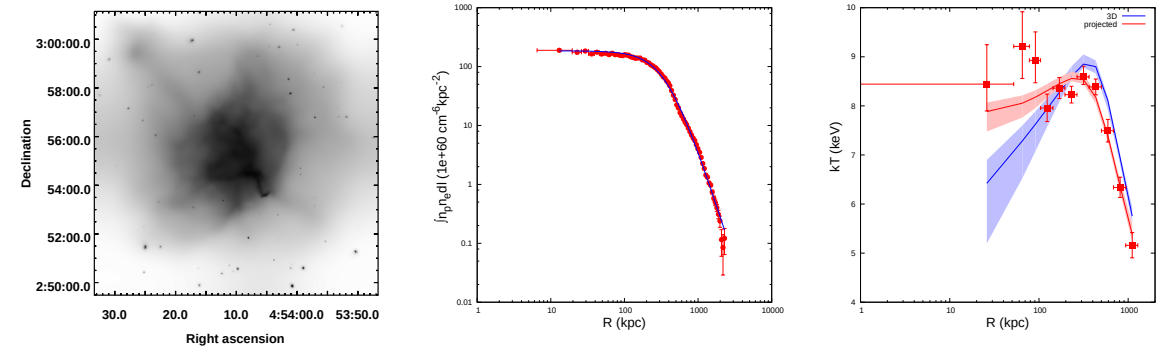

Figure C6. Same as Figure C1 but for A520.

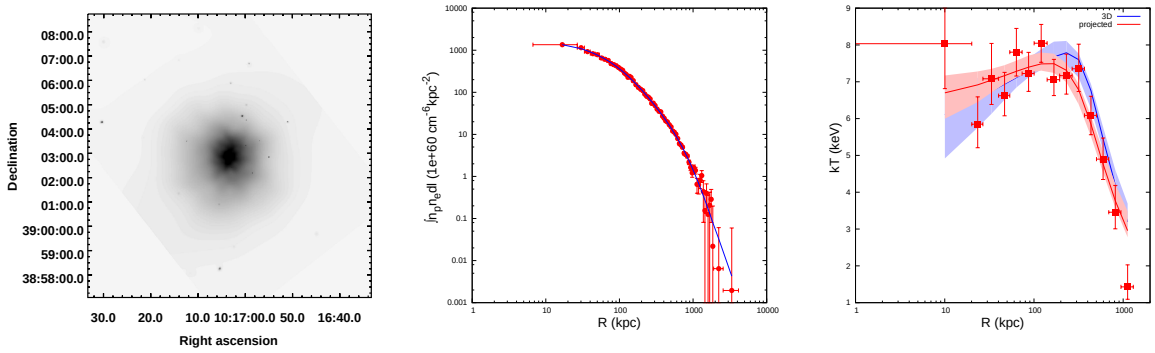

Figure C7. Same as Figure C1 but for A963.

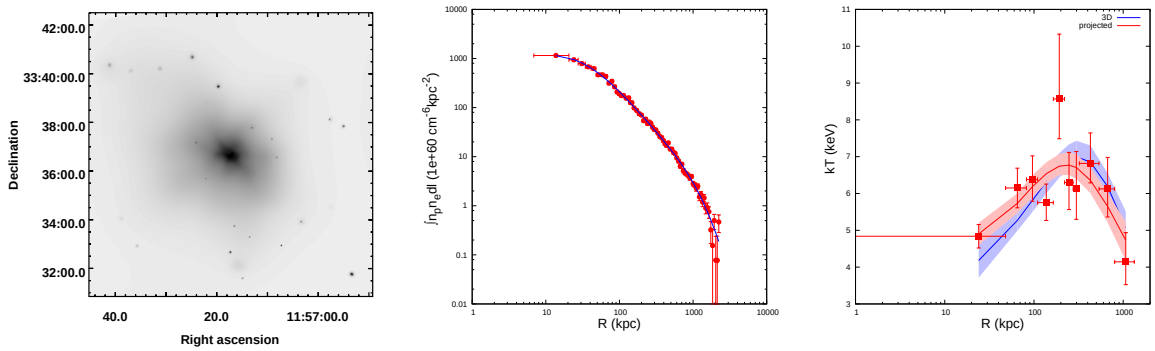

Figure C8. Same as Figure C1 but for A1423.

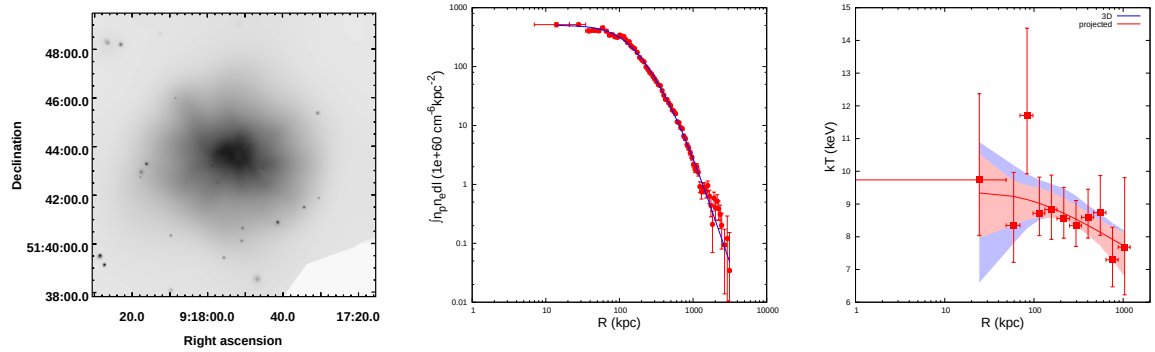

Figure C9. Same as Figure C1 but for A773.

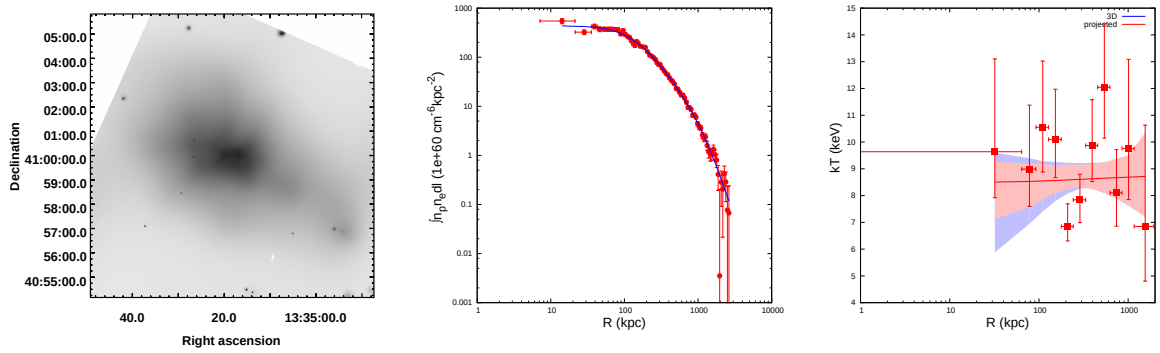

Figure C10. Same as Figure C1 but for A1763.

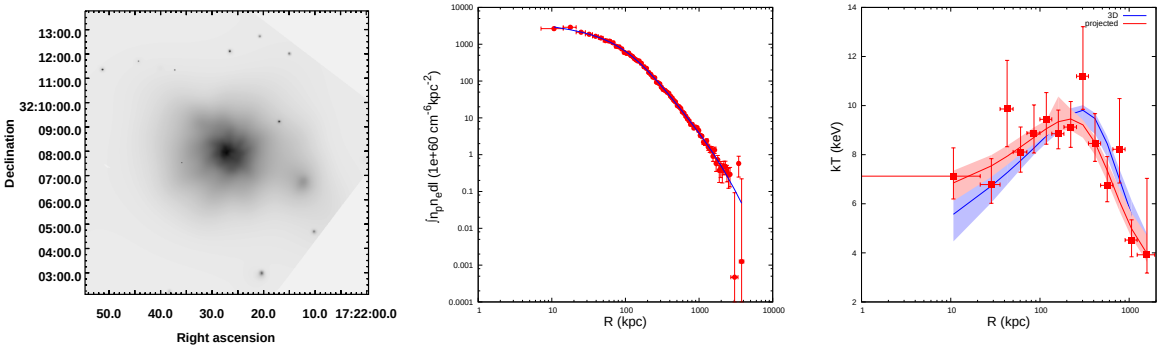

Figure C11. Same as Figure C1 but for A2261.

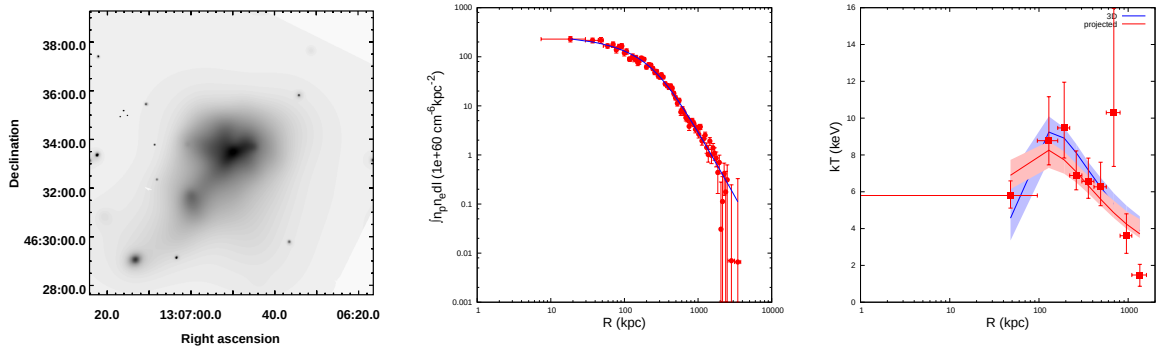

Figure C12. Same as Figure C1 but for A1682.

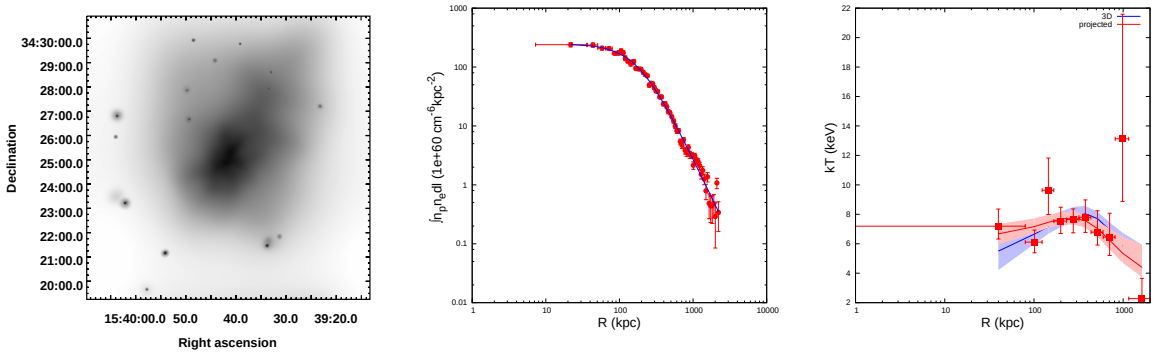

Figure C13. Same as Figure C1 but for A2111.

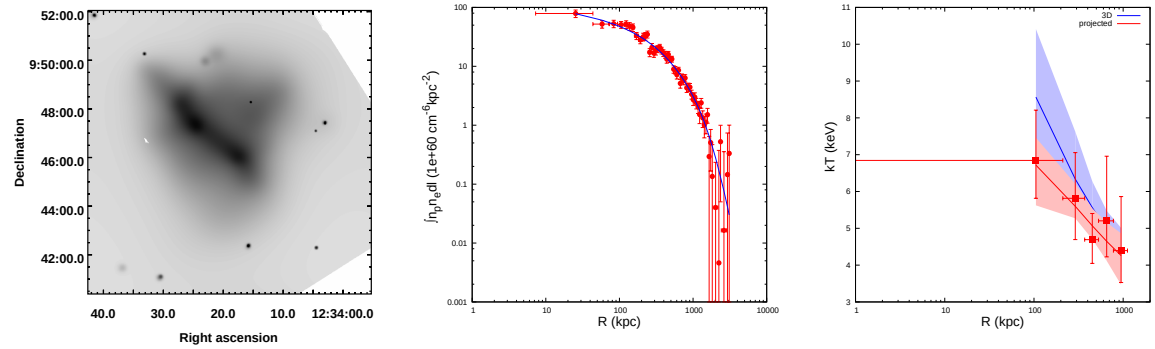

Figure C14. Same as Figure C1 but for Z5247.

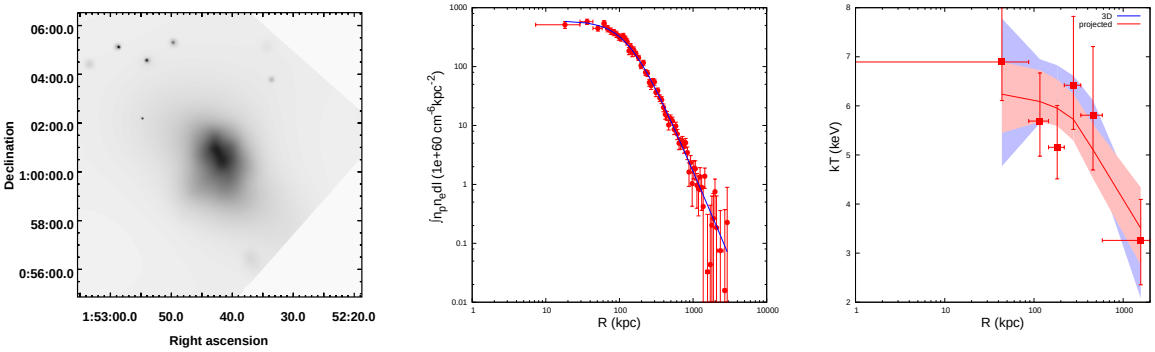

Figure C15. Same as Figure C1 but for A267.

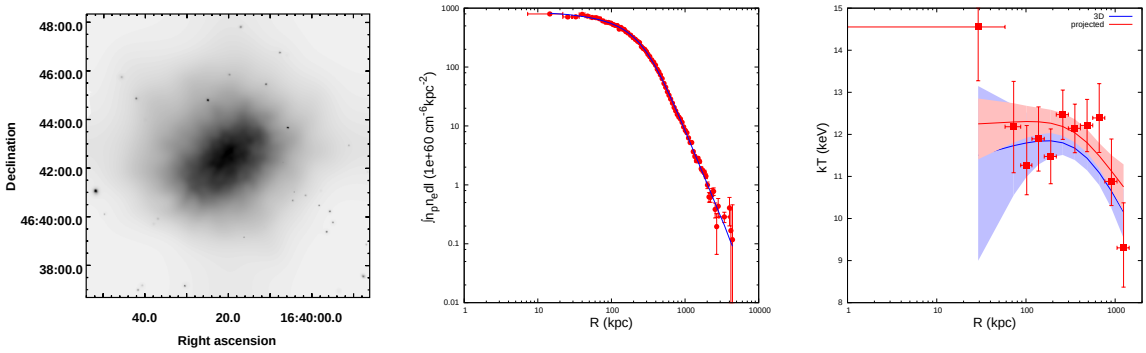

Figure C16. Same as Figure C1 but for A2219.

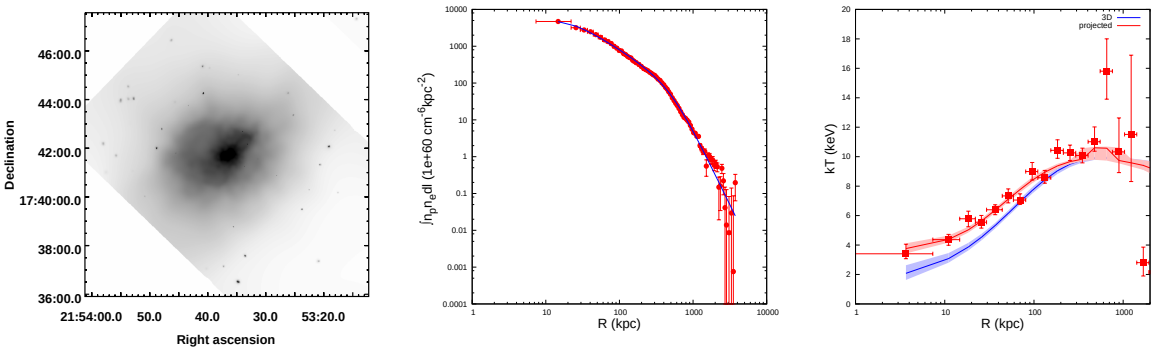

Figure C17. Same as Figure C1 but for A2390.

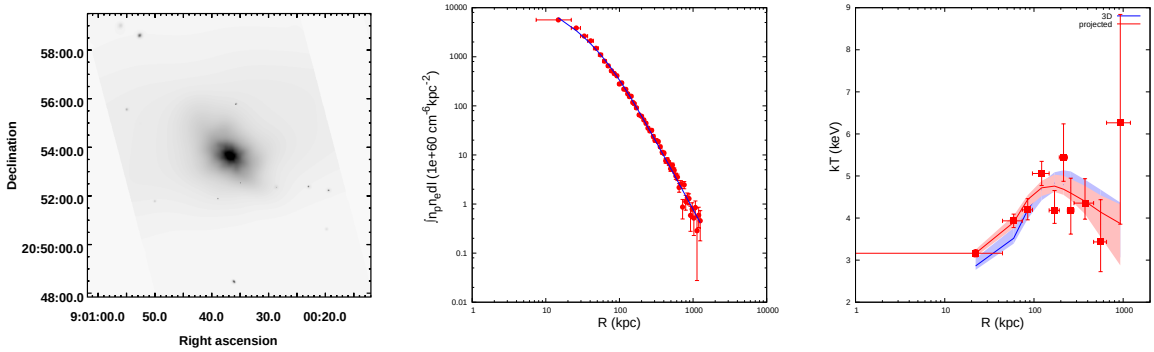

Figure C18. Same as Figure C1 but for Z2089.

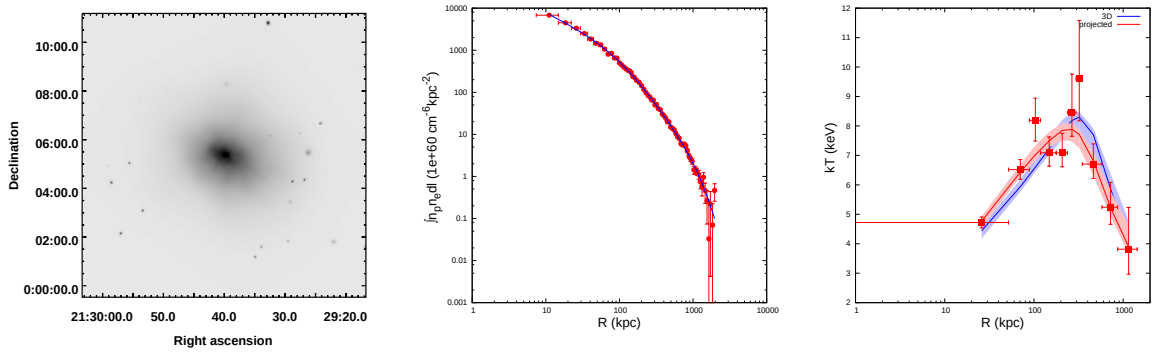

Figure C19. Same as Figure C1 but for RXJ2129.6+0005.

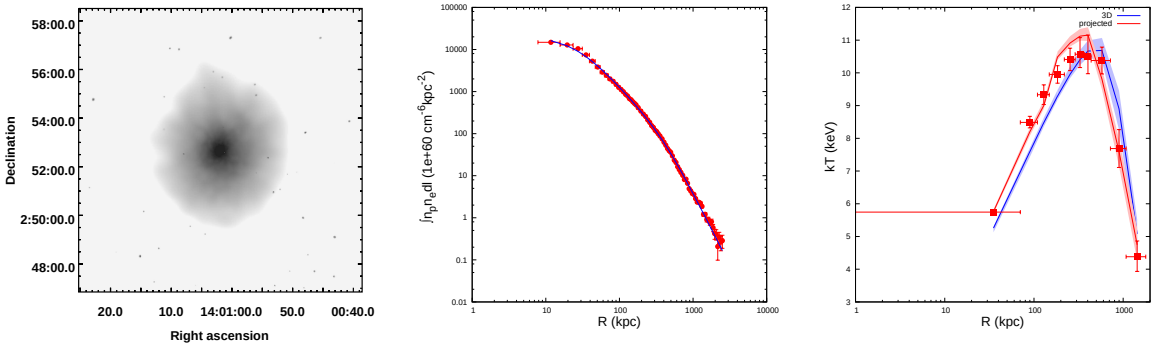

Figure C20. Same as Figure C1 but for A1835.

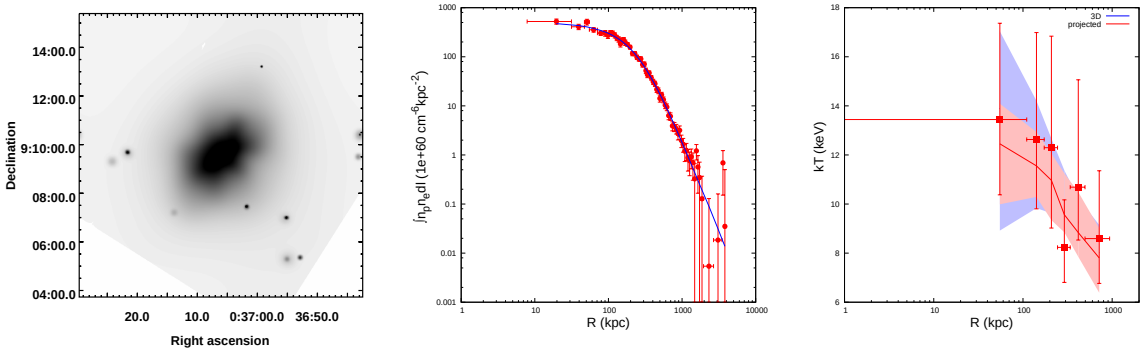

Figure C21. Same as Figure C1 but for A68.

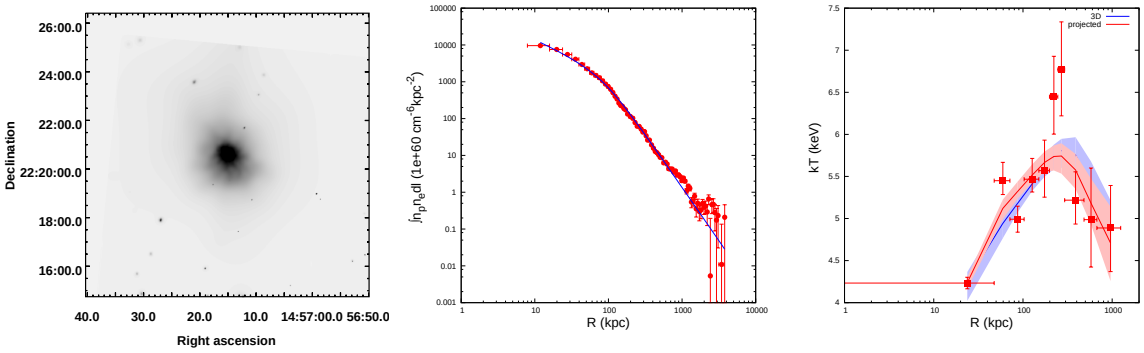

Figure C22. Same as Figure C1 but for MS1455.0+2232.

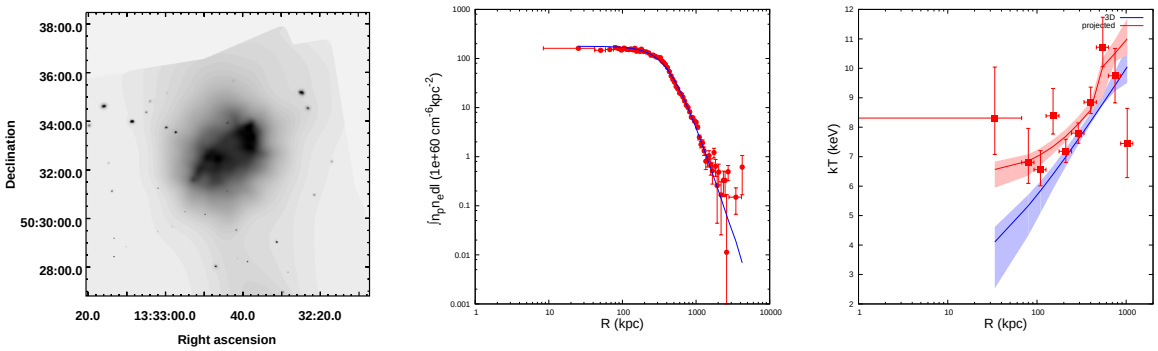

Figure C23. Same as Figure C1 but for A1758.

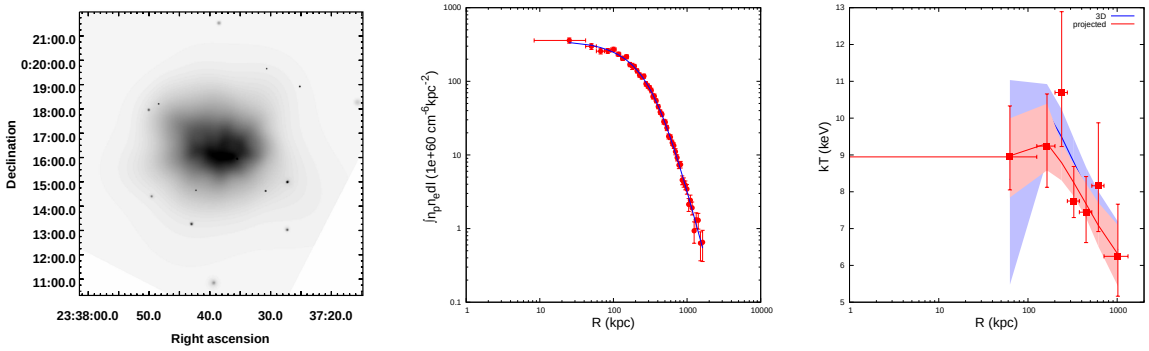

Figure C24. Same as Figure C1 but for A2631.

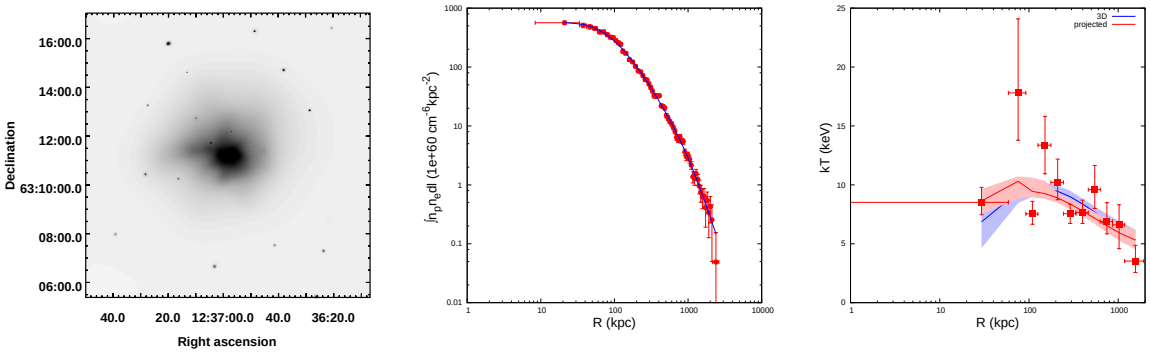

Figure C25. Same as Figure C1 but for A1576.

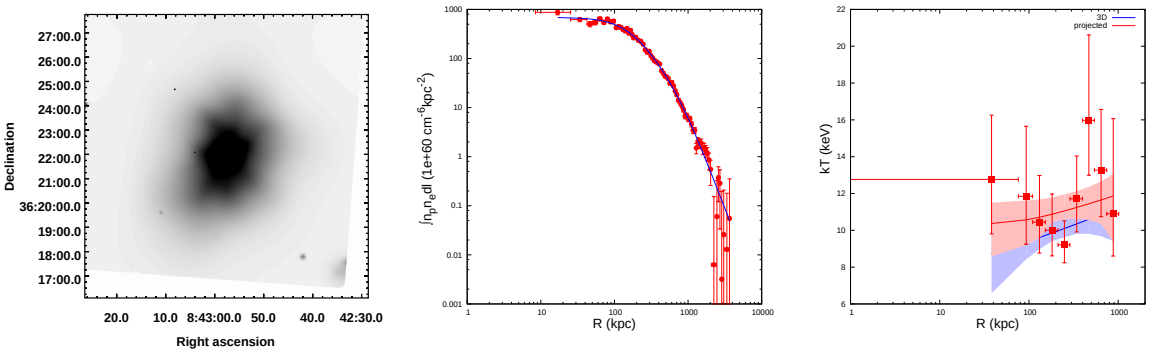

Figure C26. Same as Figure C1 but for A697.

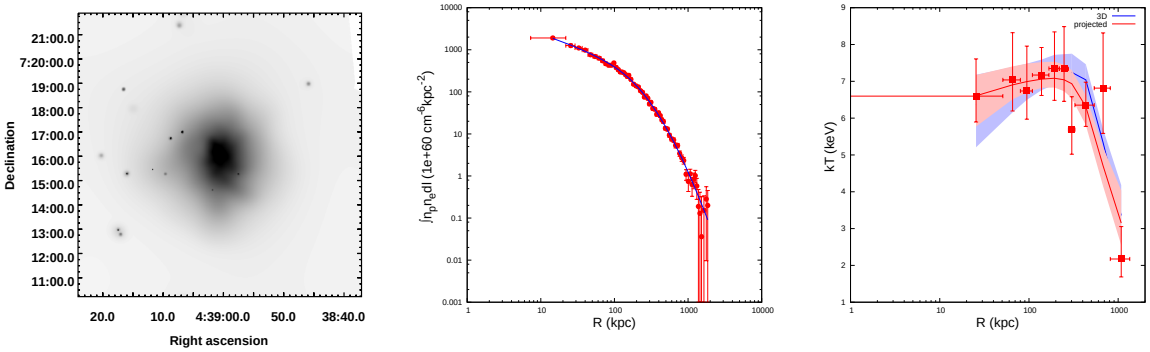

Figure C27. Same as Figure C1 but for RXJ0439.0+0715.

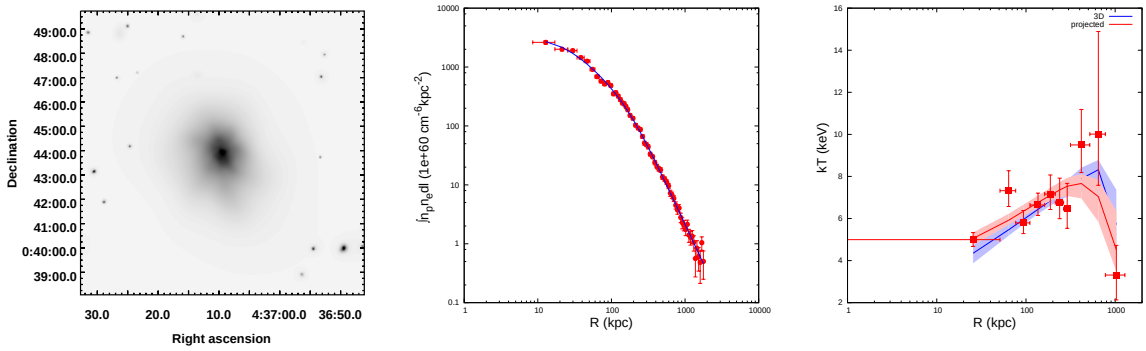

Figure C28. Same as Figure C1 but for RXJ0437.1+0043.

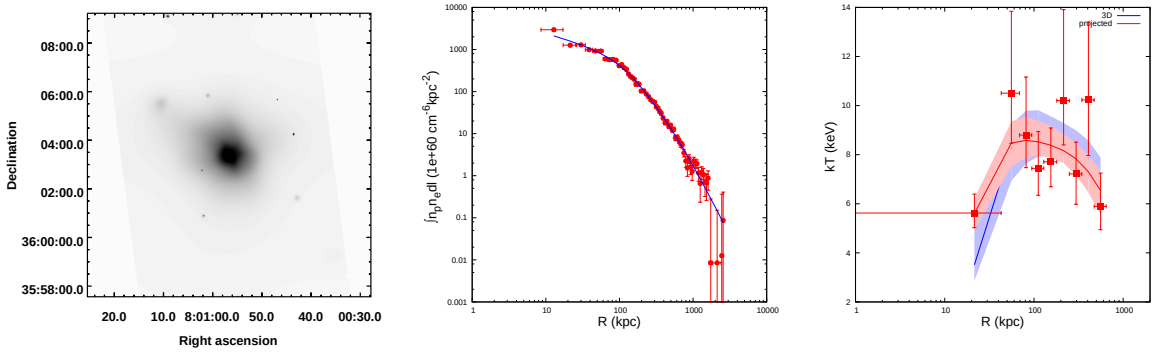

Figure C29. Same as Figure C1 but for A611.

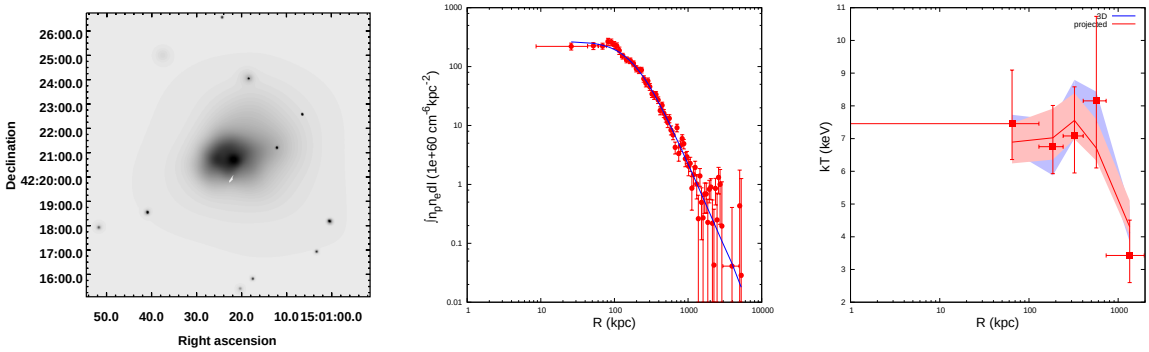

Figure C30. Same as Figure C1 but for Z7215.

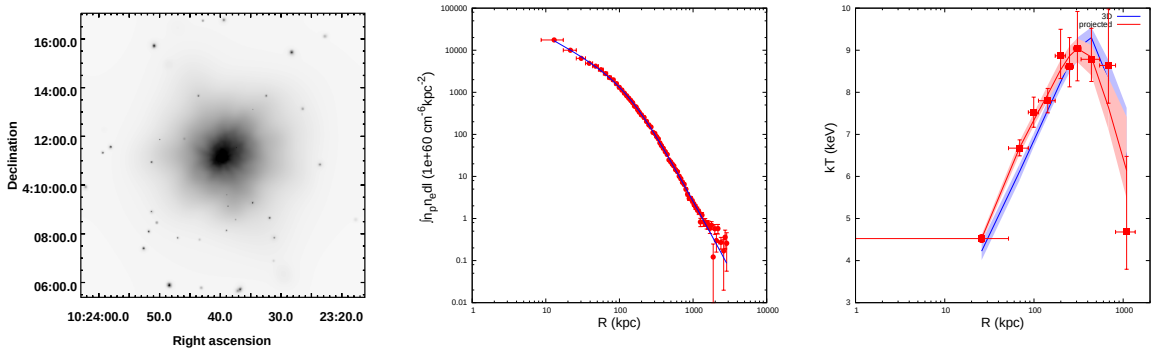

Figure C31. Same as Figure C1 but for Z3146.

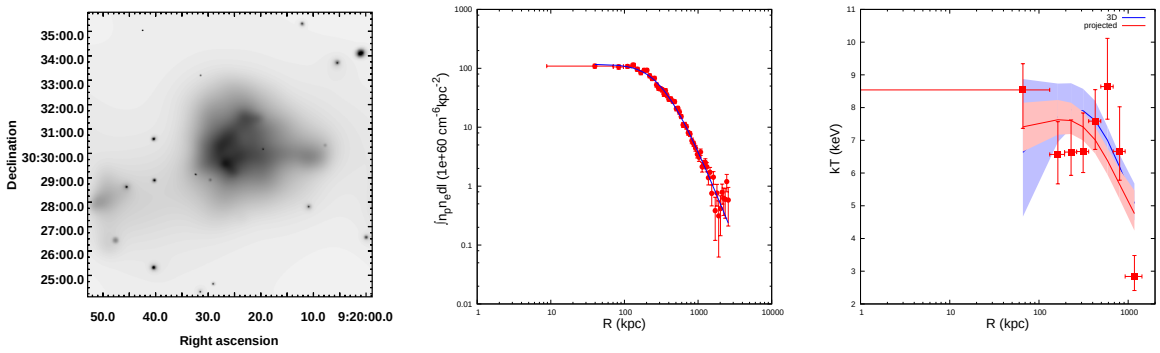

Figure C32. Same as Figure C1 but for A781.

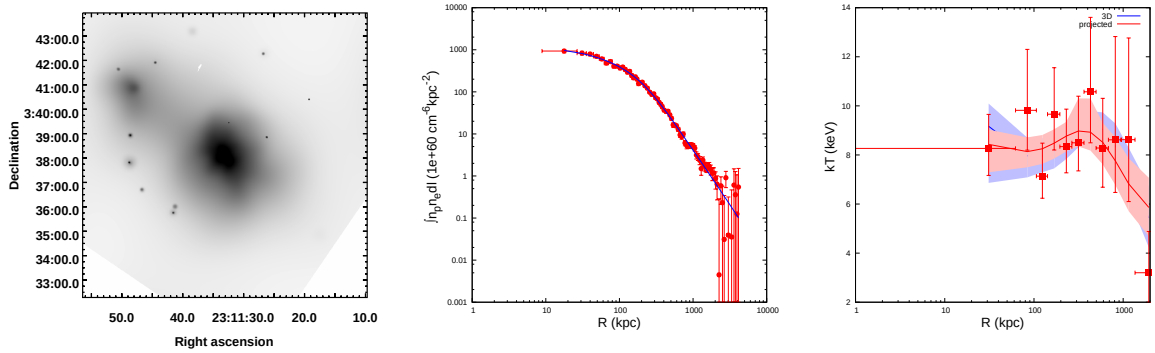

Figure C33. Same as Figure C1 but for A2552.